

# A 2163: Merger events in the hottest Abell galaxy cluster

## I. Dynamical analysis from optical data<sup>★,★★</sup>

S. Maurogordato<sup>1</sup>, A. Cappi<sup>2,1</sup>, C. Ferrari<sup>3</sup>, C. Benoist<sup>1</sup>, G. Mars<sup>1</sup>, G. Soucail<sup>4</sup>, M. Arnaud<sup>5</sup>, G. W. Pratt<sup>6</sup>,  
H. Bourdin<sup>7</sup>, and J.-L. Sauvageot<sup>5</sup>

<sup>1</sup> Laboratoire Cassiopée, CNRS, UMR 6202, Observatoire de la Côte d'Azur, BP4229, 06304 Nice Cedex 4, France  
e-mail: sophie.maurogordato@oca.eu

<sup>2</sup> INAF - Osservatorio Astronomico di Bologna, via Ranzani 1, 40127 Bologna, Italy

<sup>3</sup> Institut für Astro- und Teilchenphysik, Innsbruck Universität, Technikerstrasse 25/8, 6020 Innsbruck, Austria

<sup>4</sup> Laboratoire d'Astrophysique de Toulouse-Tarbes, CNRS-UMR 5572 and Université Paul Sabatier Toulouse III, 14 Avenue Belin, 31400 Toulouse, France

<sup>5</sup> Service d'Astrophysique, DAPNIA, CEA-CEN Saclay, 91191 Gif-sur-Yvette, France

<sup>6</sup> Max-Planck-Institut für extraterrestrische Physik, Giessenbachstrasse, 85748 Garching, Germany

<sup>7</sup> Dipartimento di Fisica, Università degli Studi di Roma "Tor Vergata", via della Ricerca Scientifica 1, 00133 Roma, Italy

Received 5 April 2007 / Accepted 6 November 2007

### ABSTRACT

**Context.** A 2163 is among the richest and most distant Abell clusters, presenting outstanding properties in different wavelength domains. X-ray observations have revealed a distorted gas morphology and strong features have been detected in the temperature map, suggesting that merging processes are important in this cluster. However, the merging scenario is not yet well-defined.

**Aims.** We have undertaken a complementary optical analysis, aiming to understand the dynamics of the system, to constrain the merging scenario and to test its effect on the properties of galaxies.

**Methods.** We present a detailed optical analysis of A 2163 based on new multicolor wide-field imaging and medium-to-high resolution spectroscopy of several hundred galaxies.

**Results.** The projected galaxy density distribution shows strong subclustering with two dominant structures: a main central component (A), and a northern component (B), visible both in optical and in X-ray, with two other substructures detected at high significance in the optical. At magnitudes fainter than  $R = 19$ , the galaxy distribution shows a clear elongation approximately with the east-west axis extending over  $4 h_{70}^{-1}$  Mpc, while a nearly perpendicular bridge of galaxies along the north-south axis appears to connect (B) to (A). The (A) component shows a bimodal morphology, and the positions of its two density peaks depend on galaxy luminosity: at magnitudes fainter than  $R = 19$ , the axis joining the peaks shows a counterclockwise rotation (from NE/SW to E-W) centered on the position of the X-ray maximum. Our final spectroscopic catalog of 512 objects includes 476 new galaxy redshifts. We have identified 361 galaxies as cluster members; among them, 326 have high precision redshift measurements, which allow us to perform a detailed dynamical analysis of unprecedented accuracy. The cluster mean redshift and velocity dispersion are respectively  $z = 0.2005 \pm 0.0003$  and  $1434 \pm 60 \text{ km s}^{-1}$ . We spectroscopically confirm that the northern and western components (A 2163-B and A 2163-C) belong to the A 2163 complex. The velocity distribution shows multi-modality, with an overall bimodal structure peaking at  $\sim 59\,200 \text{ km s}^{-1}$  and  $\sim 60\,500 \text{ km s}^{-1}$ . A significant velocity gradient ( $\sim 1250 \text{ km s}^{-1}$ ) is detected along the NE/SW axis of the cluster, which partially explains the detected bimodality. A 2163 appears to be exceptionally massive: the cluster virial mass is  $M_{\text{vir}} = 3.8 \pm 0.4 \times 10^{15} M_{\odot} h_{70}^{-1}$ .

**Conclusions.** Our analysis of the optical data, combined with the available information from X-ray observations and predictions of numerical simulations, supports a scenario in which A 2163-A has undergone a recent ( $t \sim 0.5$  Gyr) merger along a NE/SW (or E-W) axis, and A 2163-B is connected to the main complex, and is probably infalling on A 2163-A.

**Key words.** galaxies: clusters: general – galaxies: kinematics and dynamics – galaxies clusters: individual: A 2163

## 1. Introduction

A 2163 is among the richest (richness class 2, similar to Coma) and most distant Abell clusters ( $z = 0.20$ ) and presents outstanding properties at various wavelengths. Extensive X-ray observations have shown that A 2163 is the hottest Abell cluster (temperature estimates vary between 11.5 and 14.6 keV;

Arnaud et al. 1992; Elbaz et al. 1995; Markevitch et al. 1996; Markevitch & Vikhlinin 2001; Pratt et al. 2001) and is among the most luminous ( $L_X[2-10 \text{ keV}] = 6.0 \times 10^{45} \text{ ergs/s}$ , Ginga+ROSAT/PSPC, Elbaz et al. 1995). The clear subclustering in the ICM density map (Elbaz et al. 1995), in particular the presence of a clearly-resolved secondary cluster in the North (A 2163B in Elbaz et al. 1995) and the rotation of the main cluster isophotes with radius, together with strong temperature variations in the central region (Markevitch & Vikhlinin 2001; Bourdin et al. 2001; Govoni et al. 2004) are typical signatures of merging processes. The X-ray surface brightness profile of the cluster is well fitted by a  $\beta$ -model (Elbaz et al. 1995; Pratt et al. 2001) and the temperature profile was shown to be relatively flat

\* Based on data obtained with the European Southern Observatory, Chile (runs 073.A-0672 and 077.A-0813) and with the Canada France Hawaii Telescope.

\*\* Table 1 is only available in electronic form at the CDS via anonymous ftp to cdsarc.u-strasbg.fr (130.79.128.5) or via <http://cdsweb.u-strasbg.fr/cgi-bin/qcat?J/A+A/481/593>

outside the very center, with a decline at large radius (Pratt et al. 2001). The binding mass, derived from X-ray observations under the isothermal hypothesis, is very large:  $4.6^{+0.4}_{-1.5} \times 10^{15} M_{\odot}$  within a radius of 4.6 Mpc (Elbaz et al. 1995, assuming a cosmology with  $H_0 = 50 \text{ km s}^{-1} \text{ Mpc}^{-1}$ ,  $\Omega_0 = 1$ ).

The galaxy density and mass distribution in the central region of this cluster have also been determined by weak gravitational lensing (Squires et al. 1997; Cypriano et al. 2004). These analyses show very similar mass and galaxy distributions, with two coincident maxima and a flat shape elongated in the E-W direction, although the weak lensing signal is surprisingly faint in comparison to that expected from the cluster X-ray properties. However, these detailed studies are limited to the inner  $8' \times 8'$  region of the cluster, and do not include the peripheral clumps such as A 2163-B. La Barbera et al. (2004) estimated the photometric redshifts of galaxies in A 2163-B, showing that this structure lies at the typical redshift of the main cluster ( $z = 0.215 \pm 0.0125$ ).

The available optical and X-ray results suggest that A 2163 is not a completely relaxed cluster, as shown both by signatures of a merging event in the central region, and by the presence of A 2163-B, which is a possible interacting subcluster in the North, at  $\sim 7$  arcmin from the peak of X-ray emission. Radio observations (Feretti et al. 2001) revealed both an elongated, diffuse source in the N-E peripheral region of A 2163 (a possible relic), in addition to one of the most powerful and extended radio halos ever detected, which is quite regular in shape and elongated in the E-W direction, similar to the X-ray emission. Further analysis has shown that the spectral index map of the halo is flatter in a region elongated along the N-S direction and crossing the cluster centre, and at the northern and southern boundaries of the halo (Feretti et al. 2004). While the physical processes generating radio halos are still not clarified, several studies have shown that these objects are preferentially found in rich X-ray bright clusters (Giovannini et al. 2002), and the mechanism of formation is probably connected to cluster mergers (Brunetti et al. 2003; Govoni et al. 2004; Feretti 2006; Ferrari et al. 2008). A better understanding of the merging scenario in A 2163 will hopefully shed some light on the formation of its radio halo and on the origins of its clumpy spectral map.

This work is part of a more general program aiming at reconstructing the merging scenario(s) of Abell 2163 through a combined large-scale optical/X-ray analysis, and test the relation between the merging event and the properties of the galaxies and of the gas. Recent analyses of merging clusters combining a high number of redshifts with X-ray and/or radio data have brought significant insight in the understanding of these complex systems (for a non exhaustive list, see for instance Quintana et al. 1996; Biviano et al. 1996; Maurogordato et al. 2000; Arnaud et al. 2000; Flores et al. 2000; Bardelli et al. 2001; Czoske et al. 2002; Ferrari et al. 2003, 2005; Miller et al. 2004; Ledlow et al. 2005; Miller et al. 2006; Boschin et al. 2004; Girardi et al. 2005; Boschin et al. 2006; Girardi et al. 2006; Barrena et al. 2007). In this paper we present the results obtained from the analysis of our optical observations carried out in 2004 and 2006 at ESO, including wide-field multi-band imaging with the Wide Field Imager on the 2.2 m telescope, high resolution ( $R \sim 2000$ ) spectroscopy obtained with the VIMOS Spectrograph at the VLT/UT3 telescope, and older spectroscopy obtained at CFHT with the MOS instrument at lower resolution. This paper will be followed by an analysis of the X-ray observations by XMM and Chandra, focusing on the signature of the merging process in the temperature maps, and by the study of the star formation history of cluster members with respect to the merging event.

In Sect. 2 we present the data and the reduction procedure. Section 3 focuses on the projected density distributions of the galaxies and the gas, and their comparison through the determination of isodensity maps and projected density profiles. We analyse the velocity distribution and the dynamics of the whole cluster in Sect. 4, and the existence of subclustering both in density and velocity space in Sect. 5. In Sect. 6 we derive an estimate of the cluster mass and compare it to independent X-ray and weak-lensing estimates. Discussion and conclusions are presented in Sect. 7.

In the following, we adopt the cosmological parameters of a  $\Lambda$ CDM model with  $\Omega_M = 0.3$ ,  $\Omega_{\Lambda} = 0.7$  and  $H_0 = 70 \text{ km s}^{-1} \text{ Mpc}^{-1}$ . With these parameters, at  $z = 0.2$  one degree corresponds to a physical length of 11.9 Mpc.

## 2. Observations and data reduction

### 2.1. Data acquisition and reduction

Our observations were carried out at ESO in 2004 (run 073.1-0672) and 2006 (run 077.A-0813). We also used additional unpublished data from spectroscopic observations at lower resolution obtained at CFHT in 1996 (see below). A 2163 was observed with the Wide Field Imager at the ESO 2.2 m telescope and with the VIMOS (VIVisible Multi-Object Spectrograph; Le Fèvre et al. 2000) at the Melipal UT3 telescope of the ESO VLT. Imaging of the central  $30' \times 30'$  field has been performed in the  $R$  (filter ESO/878) and  $V$  (filter ESO/843) bands. For each filter eight dithered images were obtained, leading to a total exposure time of 40 mn. The seeing FWHM values of the  $R$  and  $V$  band images amount to 1.25 and 1.40 arcsec, respectively.

These sets of images were reduced and combined using the ESO/MVM package (Alambic, Vandame 2002), and the galaxy catalogs in the two passbands were extracted with SExtractor (Bertin & Arnouts 1996). These catalogs include half-light radii and magnitudes (we adopted the MAG\_AUTO estimate), and the resulting magnitude-half light radius diagram was used to classify stars and galaxies up to a magnitude of 21 in both bands. The limiting magnitudes, defined as  $5\sigma$  detections within an aperture of twice the seeing FWHM, are 22.5 and 21.5 in the  $R$ - and  $V$ -bands, respectively. Finally, the  $V$ - and  $R$ -band catalogs were matched by adopting a matching radius of 1.5 arcsec.

For multi-object spectroscopy, masks were prepared through the VMPS (VIMOS Mask Preparation Software, Bottini et al. 2005). Spectra were obtained in the  $30' \times 30'$  field covered by WFI, with VIMOS in Multi-Object Spectroscopy mode. We used the High Resolution Blue grism, with a slit of  $1''$  width, which leads to a resolution in the range  $[R \sim 2050-2550]$  and covers the wavelength range 4200–6200 Å for a centered slit. At the cluster redshift this range includes [OII],  $K$  and  $H$ ,  $G$  band,  $H_{\delta}$ ,  $H_{\gamma}$ ,  $H_{\beta}$ , [OIII]a&b among the main spectral lines. About 100 slits per pointing were assigned to targets, and the field was covered with six pointings (four obtained in 2004 and two in 2006) following a dithering pattern, in order to fill the cross-shaped gap ( $2'$  wide) among the 4 VIMOS quadrants. For each pointing, we obtained four exposures of 45 mn. The prerelation of spectroscopic data was performed with the dedicated VIPGI package (Scodreggio et al. 2005). Finally, redshifts were measured through the standard cross-correlation package *rvsao* in IRAF (Tonry & Davis 1981), using three stellar template spectra obtained during our observing runs and a set of synthetic spectra derived from the population synthesis library of Bruzual & Charlot (2003). All the spectra were checked visually for the presence of [OII], [OIII], and Balmer lines in emission with

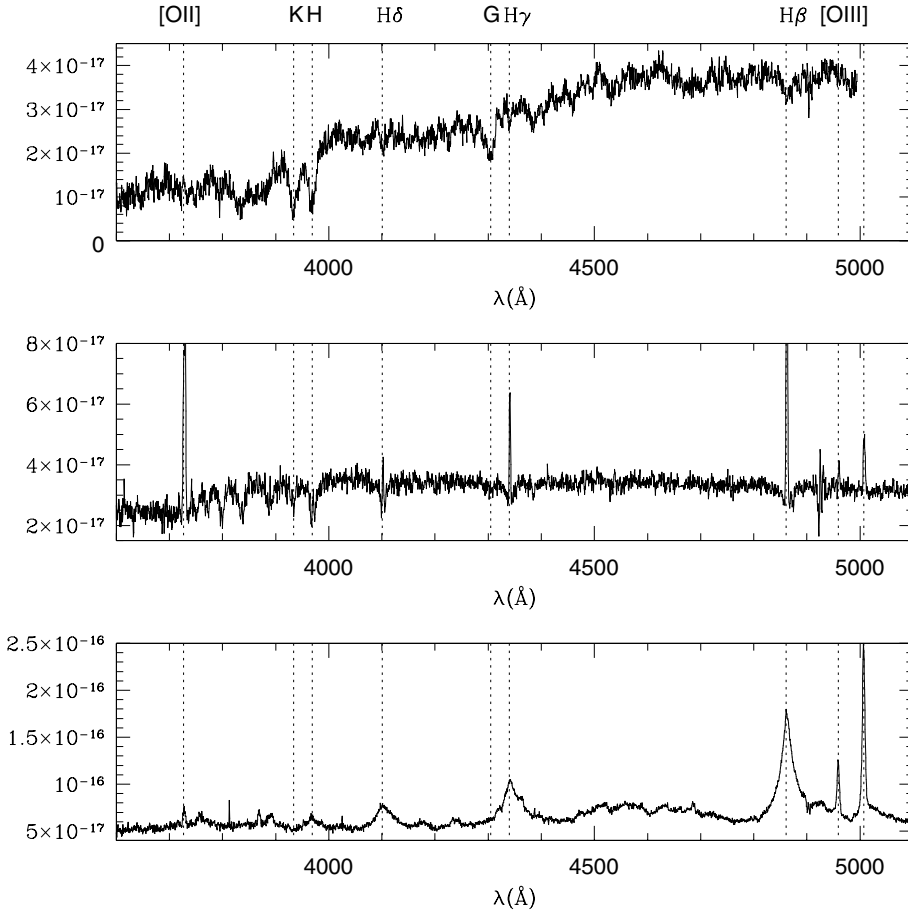


**Fig. 1.** Examples of spectra obtained with VIMOS in HR mode which are representative of our Flag 0 sample. Spectra have been deredshifted, and the rest wavelengths of various lines ([OII], Calcium K and H, H $\delta$ , G band, H $\gamma$ , H $\beta$ , [OIII]) are shown with dotted lines. Intensity values are in arbitrary units. From top to bottom: **a)** spectrum of the brightest cluster member BCG-1 (see Table 3), with absorption lines typical of an old population; **b)** spectrum of a typical emission line galaxy, with Balmer lines both in absorption and emission and oxygen emission lines; **c)** spectrum of the galaxy with X-ray emission north of A 2163-B with broad hydrogen lines, which is a type I AGN.

equivalent widths larger than 5 Å, and in case of positive detection the emission lines redshifts were measured. For galaxies where both absorption and emission redshifts were available, we selected the value with the smaller error. Redshifts are heliocentric (in our case the heliocentric correction is small, amounting to +3 km s<sup>-1</sup>).

Objects were classified in two categories according to the quality of the spectra, and thereby to the precision of the derived redshifts: a) the “high precision” sample (Flag 0), including galaxies having high *S/N* ratio spectra ( $\sim 10$  per pixel or higher) and typical redshift errors of  $\sim 20$  km s<sup>-1</sup>; b) the “medium precision” sample (Flag 1), including galaxies having lower *S/N* ratio spectra but reliable redshifts, although with larger errors ( $\sim 100$  km s<sup>-1</sup>). Examples of Flag 0 spectra are displayed in Fig. 1. The dynamical analysis was generally performed on the high precision spectroscopic Flag 0 sample; the total sample was used when the redshift precision was not critical (e.g. when associating galaxies to the cluster in the color-magnitude diagram for the best determination of the red sequence).

As we mentioned above, we use supplementary data from multi-object spectroscopy obtained at CFHT with the MOS instrument, where the grism had a dispersion of 300 Å/mm, giving a wavelength scale of 7 Å per pixel on the CCD in binned mode, and a maximum wavelength range of 4400 to 8000 Å. Due to the lower spectral resolution of CFHT observations, these objects have Flag 1. CFHT observations provided 108 spectra and 79 galaxies belonging to the cluster were identified: 51 of them were also observed with VIMOS. After applying a  $3\sigma$  clipping, the mean offset in velocity is  $-90 \pm 42$  km s<sup>-1</sup>, which is within the mean errors from the CFHT measurements. When both measurements were available, we chose the higher precision VIMOS

measurement. In total, 28 objects were added from the CFHT observations. Therefore our final spectroscopic catalog includes 512 spectra with a successful radial velocity measurement. 476 of these are galaxies: 430 have a “high precision” and 46 have a “medium precision” redshift.

The catalog is shown in Table 1, where columns are as follows: 1) identification number; 2) and 3) right ascension and declination (J2000.0); 4) radial velocity; 5) velocity error; 6)  $R_{TR}$  parameter (Tonry & Davis 1981; when  $R_{TR} > 3$  the cross-correlation redshift can be considered as reliable); 7) quality flag for the redshift (0: high precision, 1: medium precision); 8) emission lines flag (0: no emission, 1: with emission); 9) instrument (1: VIMOS at ESO/VLT; 2: MOS at CFHT).

## 2.2. Completeness

Apparent magnitudes were transformed to absolute magnitudes following:  $M = m - 25 - 5 \log_{10}(D_L) - A - K(z)$ , where  $D_L$  is the luminosity distance in Mpc,  $A$  is the galactic extinction, and  $K(z)$  is the K-correction. We note that A 2163 is in a region with strong local variations of the extinction, and that the estimate of the extinction by Schlegel et al. (1998) differs from that of Burstein & Heiles (1984). For this region La Barbera et al. (2004) have found a value for  $E(B - V)$  of 0.41, in good agreement with that of Schlegel et al. (1998), which we adopted in our work. We computed the K-correction corresponding to an elliptical galaxy at  $z = 0.2$  for the set of adopted filters; in the  $R$  (AB) passband, assuming a Schechter  $M_R^* = -21.97$  (Popesso et al. 2005), we expect  $m_R^* = 18.1$ . As the limiting magnitude of our catalog is  $R = 22.5$ , this means that we observe galaxies which are 4.4 mag fainter than  $M^*$ . Moreover, the total field covered

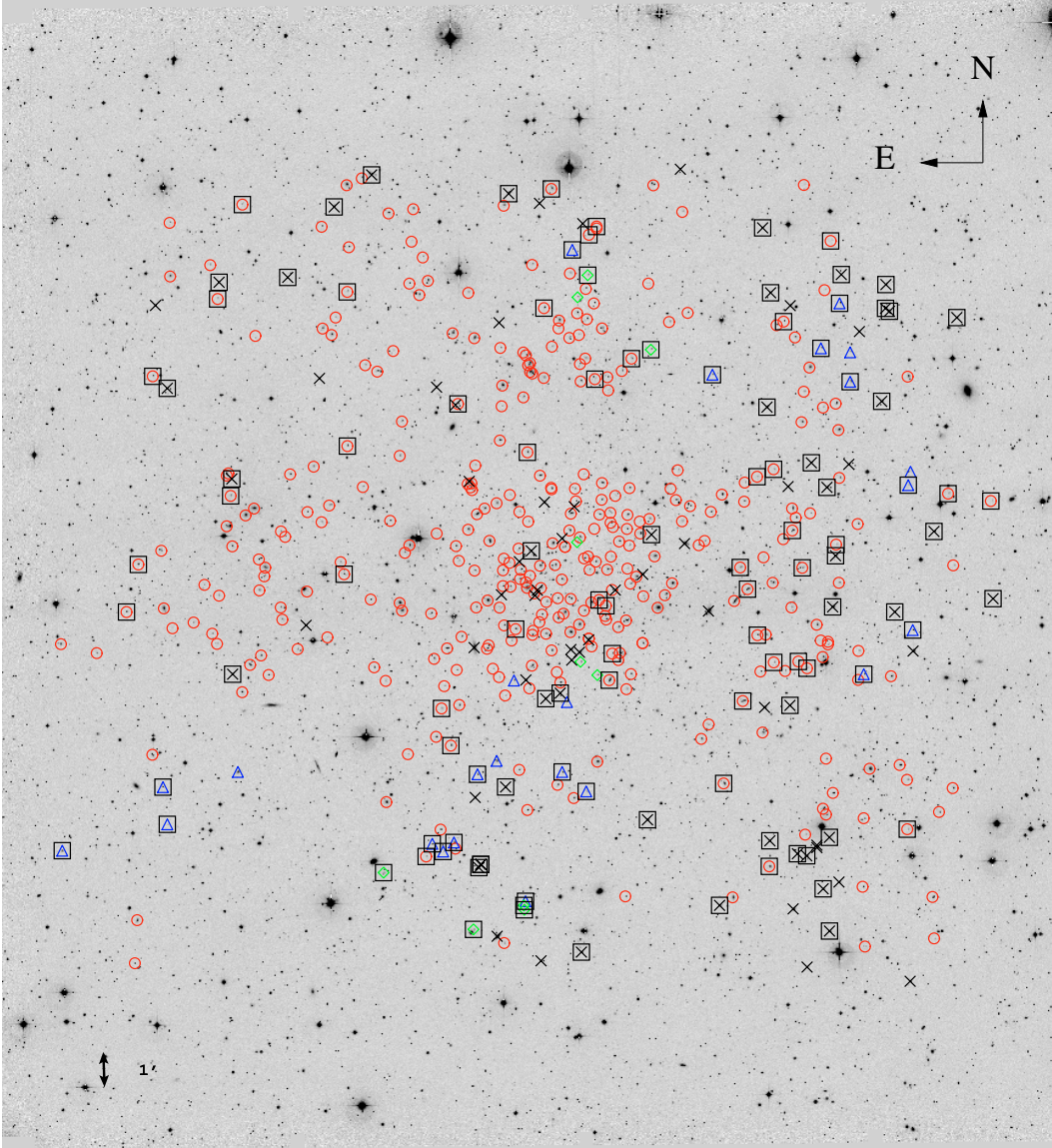


**Fig. 2.** WFI  $R$ -band image of the A 2163 field. Galaxies for which successful spectra have been obtained (Flag 0 and 1) are marked by different symbols according to their velocity. Red circles: velocity range  $[54\,000, 66\,000]$   $\text{km s}^{-1}$  corresponding to expected cluster members. Blue triangles: velocity range  $[71\,000, 77\,000]$   $\text{km s}^{-1}$  corresponding to the first background overdensity in the velocity histogram. Green diamonds: velocity range  $[87\,000\text{--}93\,000]$   $\text{km s}^{-1}$ , corresponding to the second background overdensity. Black crosses: other measured redshifts. Squares indicate emission line galaxies. There is a high number of emission line galaxies belonging to the cluster on the Western side. The spatial scale of the image is shown in the lower-left corner.

by the WFI camera ( $30' \times 30'$ ) corresponds to  $6 \times 6 \text{ Mpc}^2$  at the mean redshift of the cluster. We thus have deep, wide sampling of the galaxy population in A 2163.

The original scope of the program was to obtain spectra of all of the galaxies brighter than  $R = 20$  in the  $20' \times 20'$  region centered on A 2163, in order to sample the cluster population to luminosities  $\sim L^* + 2$ , and to a radius of  $\sim 2 h_{70}^{-1} \text{ Mpc}$ . Due to our dithering pattern and to the VIMOS field of view ( $16' \times 18'$ ), the total field covered by spectroscopy is slightly wider ( $\sim 25' \times 35'$ ), but the spectroscopic completeness in the external parts is lower. Therefore we limit the completeness analysis to the original  $20' \times 20'$  region. Figure 2 shows the the WFI  $R$ -band image of A 2163 with symbols identifying the galaxies which have a measured redshift (Flag 0+ Flag 1). We have computed the spectroscopic completeness  $f(R) = N_z(R)/N_{2D}(R)$ , where  $N_z(R)$  is the number of galaxies with a measured redshift and magnitude

brighter than  $R$ , and  $N_{2D}(R)$  is the number of galaxies in our photometric catalog with magnitude brighter than  $R$ . Figure 3 shows  $f(R)$  for our two spectroscopic catalogs, the high precision sample and the total sample, corresponding respectively to Flag 0 and Flag 0 + Flag 1 objects in Table 1. Completeness has been computed in two fields: the inner ( $8' \times 8'$ ) and the wider ( $20' \times 20'$ ). As a general trend, the wide-field completeness is stable up to  $R \leq 19.5$  and drops rapidly at higher magnitudes. In particular, the central field is highly sampled: the completeness ratio at  $R \leq 19.5$  is between 0.63 and 0.75 for the total (Flag 0 + Flag 1) sample and between 0.55 and 0.62 for the high precision (Flag 0) sample.

Figure 4 shows how the completeness at  $R \leq 19.5$  and  $R \leq 20.0$  varies in the  $20' \times 20'$  central field, computed in cells of  $2' \times 2'$ . It is clear that at both magnitudes some regions in the periphery are very poorly sampled, or even not sampled at

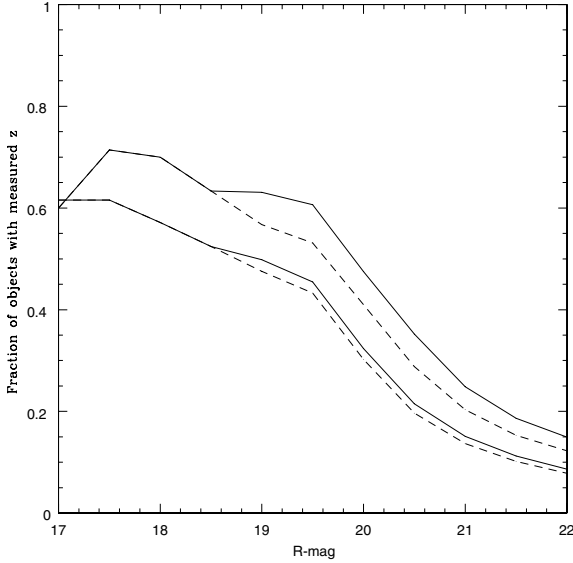


**Fig. 3.** The spectroscopic completeness of our observations as a function of  $R$ -band magnitude. Solid lines: Flag 0 + Flag 1 sample; dashed lines: Flag 0 sample. Upper and lower lines refer respectively to the  $8' \times 8'$  central field and to the  $20' \times 20'$  wide field.

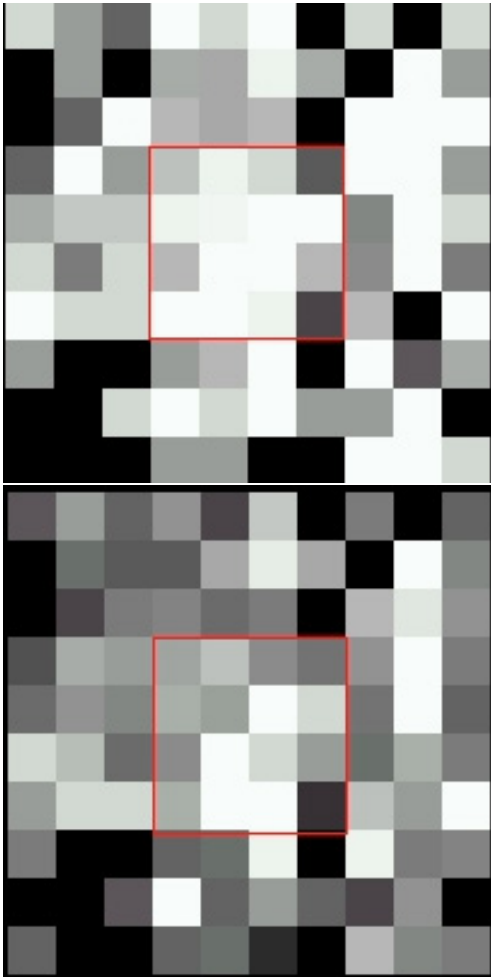


**Fig. 4.** The spectroscopic completeness map for our high precision velocity sample in the inner  $20' \times 20'$ . *Top panel:* galaxies brighter than  $R = 19.5$ ; *bottom panel:* galaxies brighter than  $R = 20$ . Individual cells are  $2' \times 2'$  wide. The completeness ratio increases from black to white. The threshold value is 0.1 for black pixels and 0.6 for white pixels. The inner field ( $8' \times 8'$ ) is displayed as a red square.

all (such as for instance the South-East and North-East corners). The main reason is due to technical problems during observations. As we have explained above, we covered the “blind cross” between the 4 VIMOS quadrants using a dithering pattern: because of several failed quadrants this pattern was not completed, as apparent from the dark pixels in the completeness map. On the other hand, some regions are very well sampled, such as the central  $8' \times 8'$  core (except in its North-West and South-West corners). Sampling is not only higher but is also more homogeneous at  $R \leq 19.5$  than at  $R \leq 20$ , in particular in the central region.

### 3. Density distribution of galaxies

#### 3.1. Projected isodensity maps

The projected density distribution of galaxies has been computed from the photometric galaxy catalog in the  $R$  band through the multi-scale algorithm of Slezak et al. (in prep.; see also Fadda et al. 1998; Ferrari et al. 2005, for a description of the algorithm). Density maps for different cuts in the  $R$  magnitude (from  $R < 19$  to  $R < 21$ , and for  $19 < R < 21$ ) are shown in Fig. 5 (top panel), where at each scale only structures which are detected at  $3\sigma$  significance above the background are visualized. The  $R < 21$  density map is superimposed on the WFI  $R$  image in Fig. 6, where the most significant substructures are identified. A visual inspection of the isodensity maps at the different magnitude cut-offs reveals a main, central component (A), while at larger distances there are a variety of substructures, the most significant lying at  $\sim 7$  arcmin North (B), with another less prominent substructure located at  $\sim 9$  arcmin East of the center (C). These three components are visible at all magnitude cut-offs. At  $R < 20$  and at fainter cut-offs, new substructures are visible, such as (D) which is  $\sim 6$  arcmin to the west of the centroid, and (E) which is  $\sim 4$  arcmin to the south of it. Other smaller substructures in the nearby periphery of the main subcluster (A) depend on the magnitude cut-off and might be spurious substructures. We note however the presence of two substructures, more prominent at fainter magnitudes, toward the northern periphery of the main subcluster (A). At faint magnitudes ( $19 < R < 21$ ), a bridge of faint galaxies connects the main subcluster (A) to the northern subcluster (B). There is also a long, low density structure including D, the main subcluster A and C, extending in the E-W direction.

The inner structure of A changes significantly with luminosity: it has an elongated shape and is bimodal, with two main components (A1 and A2 in Fig. 6) visible at all magnitudes. However, when including fainter objects, the position of A1 and A2 changes, with a counterclockwise twisting of the axis joining them: at  $R < 19$  the two density peaks are aligned along a NE/SW direction, but at fainter limiting magnitudes ( $R < 20$  and  $R < 21$ ), A1 and A2 are lying on the (E-W) large-scale axis of the cluster (Fig. 5). The angular separation of the two peaks is 2 arcmin (3.5 arcmin) in the case of bright (faint) objects. The coordinates of these maxima as a function of magnitude are listed in Table 2.

The projected density distribution of the second main component, A 2163-B, also varies with magnitude. At  $R < 19$  it has a regular, circular shape but at fainter magnitudes it becomes more elongated, with two tails extending in the NE and NW directions, respectively.

On large scales, two main orientations clearly appear at fainter magnitudes: an E-W axis, corresponding to the large-scale orientation of the main component A, and including also

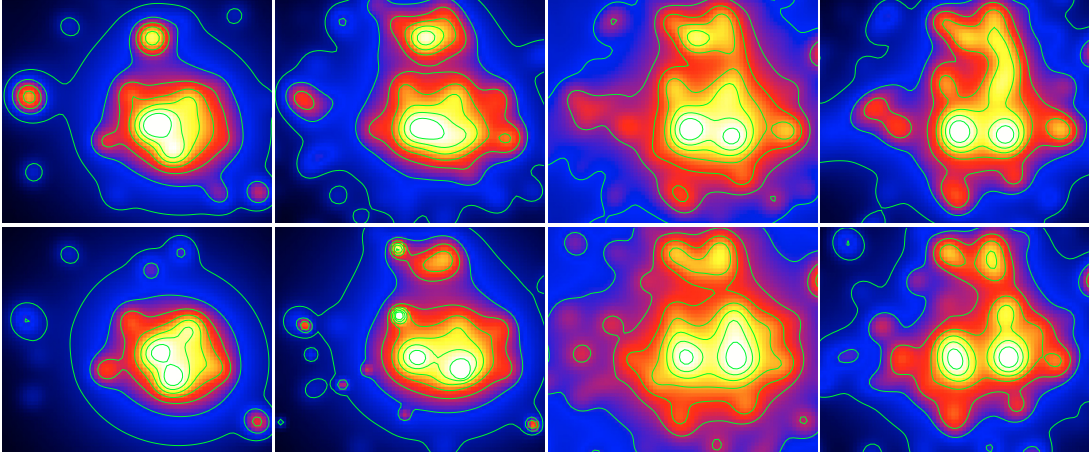


**Fig. 5.** Projected galaxy density maps for different magnitude cuts in the  $R$ -band (from left to right:  $R < 19$ ,  $R < 20$ ,  $R < 21$ , and  $19 < R < 21$ ). In the *top panels* no color selection has been applied, while in the *bottom panels* only red-sequence galaxies have been used to compute the density maps (see text). The field displayed in each panel corresponds to the central  $15' \times 20'$ . As usual, North is on the top and East on the left.

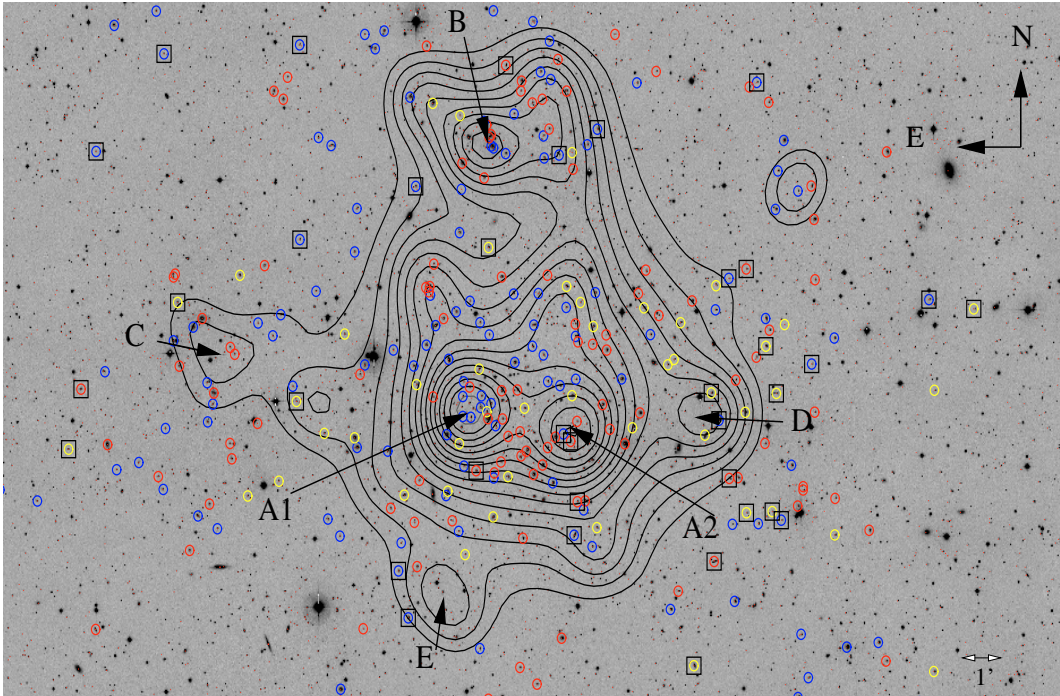


**Fig. 6.** Projected galaxy density maps for  $R < 21$  superimposed on the WFI  $R$ -band image. Substructures significant at more than the  $3\sigma$  level are identified with capital letters. Cluster members in the three velocity bins corresponding to the KMM partitions are marked with circles of different colors. Blue: KMM1; red: KMM2; yellow: KMM3. Emission line galaxies are indicated with a black square.

the C and D substructures, and a N–S axis, joining the northern subcluster B, the main component A, and the E substructure.

In order to better isolate the cluster population of early type galaxies, we used our photometric data to construct the color-magnitude diagram and to identify the red sequence of A 2163. The resulting density map has the advantage of being largely decontaminated of projection effects, and can be considered as more representative of the true cluster density map (although it will obviously miss concentrations dominated by objects with late-type or peculiar colors). We have plotted the  $(V-R)$  versus  $R$  diagram of galaxies: a) in the central  $10' \times 10'$  region (Fig. 7, top panel); b) in the whole  $30' \times 30'$  field covered by the WFI (Fig. 7, bottom panel); c) with velocities within the cluster range (Fig. 8). In all diagrams the red sequence is clearly visible at  $R < 20$  (with an obviously higher dispersion when including the whole

**Table 2.** Coordinates of the maxima in the projected galaxy isodensity maps and in the ROSAT X-ray image (Elbaz et al. 1995) of A 2163. As the positions of the maxima in the central subcluster A 2163-A, A1 and A2, depend on the limiting  $R$ -band magnitude, two sets of values are listed, corresponding to  $R \leq 19$  and  $R \leq 21$ , respectively.

Subcluster	Limiting $R_{\text{mag}}$	RA (J2000)	Dec(J2000)
A1	$R \leq 19$	16 15 47.8	-06 08 11
A2	$R \leq 19$	16 15 42.5	-06 09 53
B	$R \leq 19$	16 15 48.8	-06 02 21
C	$R \leq 19$	16 16 22.8	-06 06 17
D	$R \leq 19.5$	16 15 27.9	-06 09 18
A1	$R \leq 21$	16 15 50.9	-06 08 29
A2	$R \leq 21$	16 15 39.3	-06 09 15
X-ray (main)	–	16 15 46.0	-06 08 55
X-ray (North)	–	16 15 48.0	-06 02 25

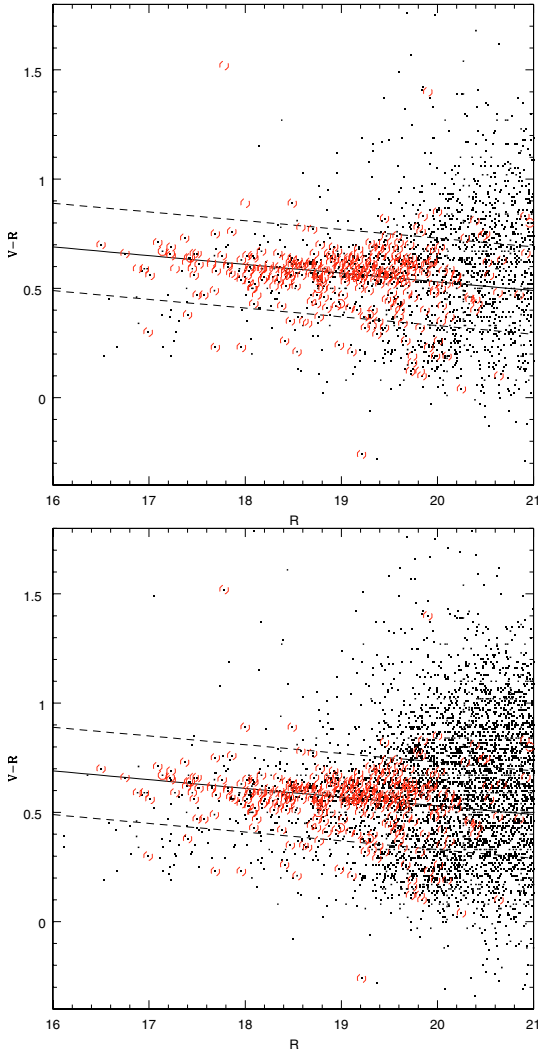


**Fig. 7.** Color–magnitude diagram in the field of A2163. *Top panel:* the central  $10' \times 10'$  field. *Bottom panel:* the whole  $30' \times 30'$  field covered by WFI. Black dots: galaxies in the photometric catalogs; red circles: spectroscopically confirmed cluster members. The solid line represents the Red Sequence best fit, while dashed lines indicate the  $\pm 2\sigma$  limits from the best fit.

field). In order to parameterize the red sequence (hereafter RS), we have used the robust fitting method introduced by Lopez-Cruz et al. (2004), fixing the magnitude cut-off at  $R = 20$ , which corresponds to  $M^* + 2$  at the cluster redshift. The values of the slope and intercept found by the minimization for these different subsamples are very stable.

In Fig. 9, the optical isodensity contours for the RS galaxies with  $R < 19$  (top) and  $R < 20$  (bottom) are superimposed on the  $R$ -band image of the central cluster region. The presence of bimodality (clumps A1 and A2 in Fig. 6) is striking, as is the twisting of the axis joining the two density peaks as a function of the magnitude cut. In both cases the peak of X-ray emission is located between the two central maxima (see the angular coordinates of the X-ray and optical subclusters listed in Table 2). It is important to stress that the two Brightest Cluster Galaxies (BCG1 and BCG2 in Fig. 9 and Table 3) are both located in the central clump A, but their positions do not coincide with the maxima of the density peaks. However, while BCG1 is near A1 (at bright and faint magnitudes), BCG2 has a significant offset to the west of A2. The axes of these two giant galaxies

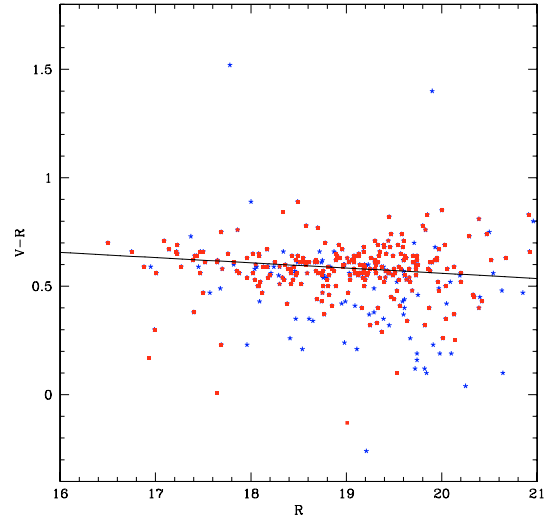


**Fig. 8.** Color–magnitude diagram for cluster members identified by spectroscopy. Red symbols indicate spectra with no emission lines while blue symbols correspond to spectra with emission lines. The solid line is the best-fit obtained applying the robust method of Lopez-Cruz et al. (2004) to the subsample of galaxies without emission lines.

and the line joining them are aligned along the same direction of the large-scale cluster density distribution, i.e. the E-W direction (see Table 3). We note the presence of a bright galaxy in proximity (east) of A2, which is also on the E-W axis.

We next fitted the RS selecting only the “redshift confirmed” cluster members as defined in Sect. 4. The color–magnitude diagram of this sample is shown in Fig. 8, both for emission lines (blue symbols) and with no emission lines (red symbols) galaxies. Emission line galaxies were excluded from the fit as they are not expected to populate the RS. The best fit parameters for the RS relation  $V - R = a + bR$  of this subsample are:  $a = 1.04$  and  $b = -0.024$ , with a  $\chi^2$  value of 0.10.

In order to construct the projected density distribution of the cluster, we selected all galaxies (with and without a measured redshift) within  $\pm 2\sigma$  from the RS best fit, assuming that they are early-type cluster members (see Fig. 7).

The density maps derived from these data are displayed in Fig. 5 (bottom panels). The overall morphology of the cluster is globally unchanged, showing the main central cluster A 2163-A and the northern subcluster A 2163-B. The density contrast of A 2163-A is enhanced in the red sequence (hereafter RS) density maps. However, this is not the case for the smaller clumps: while A 2163-E is still visible, A 2163-C and A 2163-D are hardly distinguishable. We have verified that several galaxies in clumps C and D still follow the cluster red sequence, but with a somewhat larger dispersion than that found for galaxies in the cluster central region. We conclude that the clumps C, D and E all belong to the A 2163 complex, and that their galaxy population includes both bright early type RS galaxies and fainter objects with colours outside the red sequence.

To summarize, the galaxy density distribution of A 2163 shows:

- a main cluster component (A) elongated along an E-W axis on large scales, and a northern subcluster (B), visible both in optical and in X-ray;
- several peripheral clumps; the two most significant, (C) and (D), are located east and west of the cluster centroid respectively, on the same E-W axis defined by the large scale

**Table 3.** The properties of the two brightest elliptical galaxies in the central region of A 2163, BCG-1 and BCG-2. Column 1) Identifier; Cols. 2) and 3) Right ascension and declination (J2000.0); Col. 4)  $R$ -band magnitude; Cols. 5) and 6) Radial velocity and its error; Col. 7) Position Angle of the major axis (anti-clockwise from the E-W axis).

Name	RA(J2000)	Dec(J2000)	$R$	Vel(km s <sup>-1</sup> )	Error(km s <sup>-1</sup> )	PA
BCG-1	16 15 48.9	-06 08 41	16.86	60361	10	5.
BCG-2	16 15 33.5	-06 09 16	16.45	60006	13	-9.

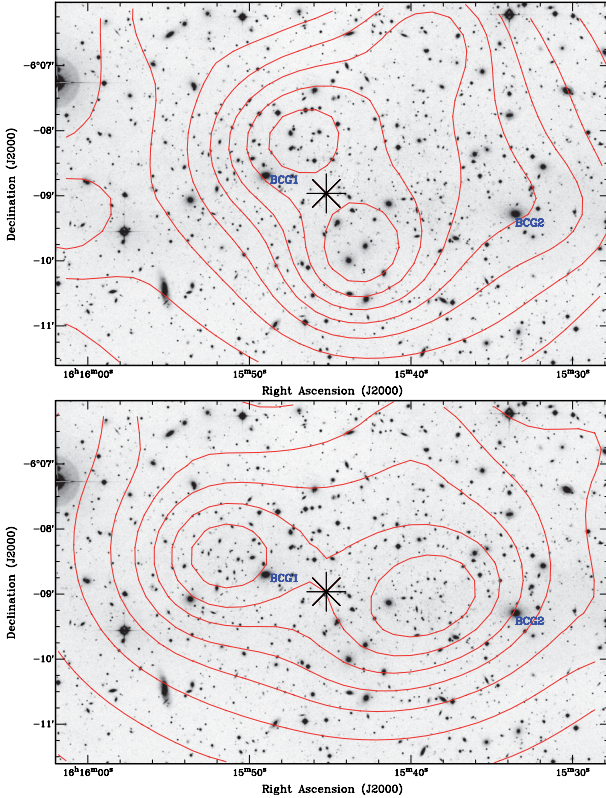


**Fig. 9.**  $R$ -band image of the central field of A 2163, showing the two BCGs (marked in figure). Contours correspond to the projected density distribution of Red Sequence galaxies with  $R < 19$  (top panel) and  $R < 20$  (bottom panel). The position of the X-ray emission peak derived from the XMM/EPIC observation is indicated by an asterisk.

distribution of A 2163-A. At faint magnitudes, a southern clump (E) appears on the N–S axis joining (A) and (B);

- a bimodal morphology (clumps A1 and A2) in the central ( $10' \times 10'$ ) cluster field;
- a significant counterclockwise twisting of the axis joining the highest density peaks of the central clumps A1 and A2 when including fainter magnitude objects;
- both the major axes of BCG1 and BCG2 and the axis joining them lie on the same E-W axis of the larger-scale cluster structure, which is seen both in the optical and X-ray maps;
- a clear offset between a) the positions of the BCGs, b) the peaks in the projected galaxy density maps and c) the X-ray intensity peak.

### 3.2. Comparison of galaxy/gas density distribution

The comparison between the galaxy and projected gas density is important to characterize the dynamical state of the cluster, as the relative distribution of the collisional versus

non-collisional components of the cluster is indicative of its merger stage (Roettiger et al. 1997).

As the projected galaxy density distribution changes with magnitude, we compare the two density maps limited at  $R < 19$  and  $R < 21$  (shown previously in Fig. 5) to the XMM/EPIC images. Using archival XMM data (ID-0112230601, ID-0112230701, ID-0112230801, ID-0112230901 and ID-0112231001) we have built a mosaic image of the cluster in the [0.5–2.] keV energy band (all instruments and pointings summed together). The isocontours of the X-ray image superimposed on the galaxy density distribution are shown in Fig. 10.

While A 2163-A and A 2163-B are detected both in optical and in X-ray, the western and eastern clumps A 2163-C and A 2163-D are not detected in X-ray. At both magnitude limits, the galaxy density distribution in A 2163-A is elongated and bimodal; although the gas distribution is centrally peaked and more regular, at large scales it exhibits the same E-W elongation seen in the optical data.

In the case of bright galaxies ( $R < 19$ ), the projected galaxy density distribution in the central region is nearly aligned with the inner major axis of the X-ray map (NE/SW), and is perpendicular to the compressed X-ray contours in the SW region which correspond to the position of the secondary optical clump A2. At large scales, the gas distribution presents the same E-W elongation as the galaxy distribution at faint magnitudes ( $R < 21$ ) (with A 2163-A, A 2163-C and A 2163-D embedded in the E-W structure). As we have seen, faint galaxies also follow the same E-W orientation in the central cluster region.

Independent of the magnitude cutoff, the position of the X-ray center does not correspond to any of the two optical maxima, but is located between them; moreover, the positions of the two BCGs correspond neither to the gas density maximum nor to the galaxy density maximum. These facts suggest that the gas is in a somewhat more relaxed state than the galaxies and that we are witnessing a post merger event in A 2163-A. In contrast, in the northern component A 2163-B the distributions of bright galaxies and of the gas are comparable, a fact which might suggest that A 2163-B has not yet collided with A 2163-A. We will discuss the merging scenario further in Sect. 7.

### 3.3. Density profiles

We have estimated the projected radial density profile in the  $30' \times 30'$  WFI field centered on the cluster. In order to correct for the areas which have been masked due to the presence of bright saturated stars, we have generated a random catalog reproducing the same geometry as observed.

We have calculated the number of objects in concentric circles of radius  $\theta$  in the galaxy catalog,  $N_{\text{gal}}(\theta)$ , and in the random catalog,  $N_{\text{rand}}(\theta)$ , deriving the projected density profile  $\sigma(\theta)$ :

$$\sigma(\theta) = \frac{N_{\text{gal}}(\theta)}{N_{\text{rand}}(\theta)} \frac{N_{\text{rand}}^{\text{tot}}}{N_{\text{gal}}^{\text{tot}}} \quad (1)$$

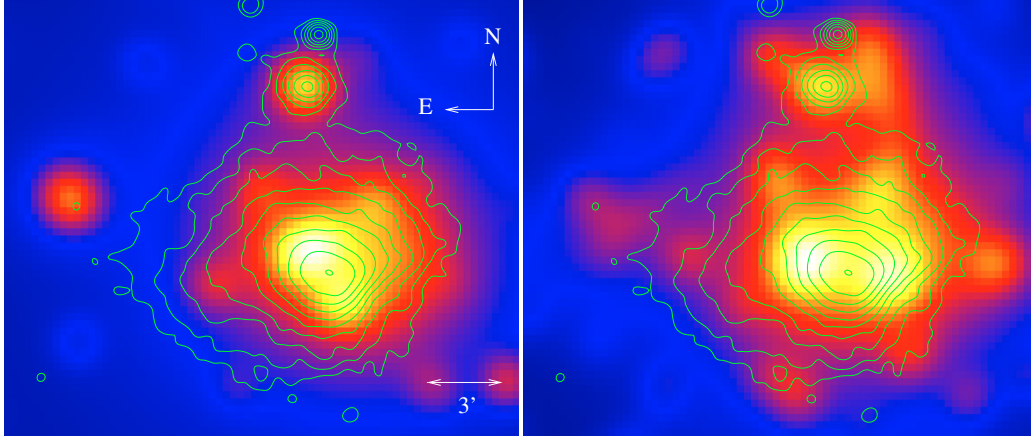


**Fig. 10.** X-ray isocontours superimposed on the projected density maps of galaxies with  $R < 19$  (left panel) and  $R < 21$  (right panel). The X-ray contours are derived from smoothed [0.5–2. keV] vignettted corrected XMM/EPIC images, and are logarithmically spaced by 0.2 dex, with the lowest contour at  $4.65\text{E-}3$  ct/s/arcmin<sup>2</sup> and the highest at  $1.86\text{E-}1$  ct/s/arcmin<sup>2</sup>.

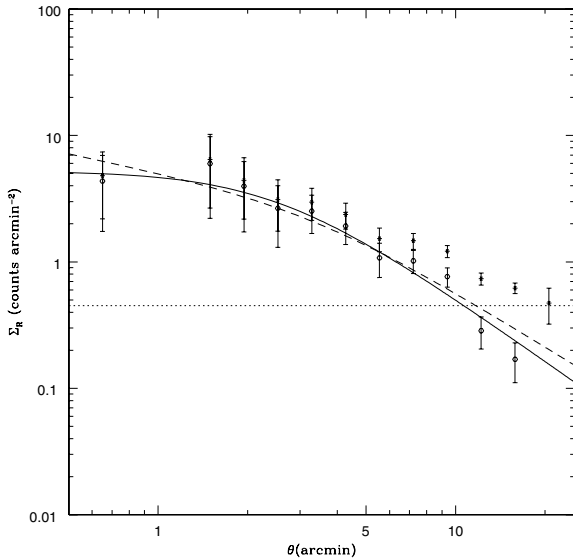


**Fig. 11.** Projected galaxy density profile in the central field of A 2163, derived from galaxies with  $R \leq 20$  belonging to the Red Sequence of the cluster. The raw profile (stars) and the background-subtracted profile (open circles) are plotted. The horizontal short dashed line marks the estimated background value. The best-fit generalized beta (solid line) and cusped models (dashed line) are also shown.

where  $N_{\text{gal}}^{\text{tot}}$  and  $N_{\text{rand}}^{\text{tot}}$  are the total number of objects in the galaxy catalog and in the random catalog, respectively. We fixed  $N_{\text{rand}}^{\text{tot}} = 200\,000$ , a value large enough to avoid introducing additive noise in the profiles.

We have fixed the cluster center at the position of the X-ray centroid, which is located between the local galaxy distribution maxima A1 and A2, and roughly coincides with the centroid of the galaxy distribution when smoothing over large scales. The profile was calculated for RS galaxies with  $R < 20.0$ , in order to minimize the contribution of the background. The estimate of the background level (critical on large scales) was calculated within a circular annulus comprised between 15 and 20 arcmin from the cluster center. Apparently the background is reached near the edge of our field.

The background subtracted profile was fitted with a generalized beta model:  $\sigma(r) = \sigma_0 / (1 + (r/r_c)^2)^\beta$  and a generalized cusped profile:  $\sigma(r) = \sigma_0 / (r/r_c (1 + (r/r_c)^2)^\beta)$ , as defined in

Adami et al. (2001), using a Levenberg-Marquardt  $\chi^2$  algorithm, which gives simultaneously the three parameters  $\sigma_0$ ,  $r_c$  and  $\beta$ .

The raw and the background subtracted radial profile and best fitting models are plotted in Fig. 11. Both the beta and cusped models provide a good fit to the data up to  $\sim 10$  arcmin, with  $\chi^2$  values of 0.25 and 0.35, respectively (the points which deviate the most – at the  $1\sigma$  level – are those at large radius, where the uncertainty due to the background subtraction is larger). For the beta model we find  $\beta = 0.83 \pm 0.15$  and  $r_c = 2.5 \pm 0.5$  arcmin, corresponding to  $r_c = 0.5 \pm 0.1$  Mpc (in our cosmology), which is a high value. In the case of a cusped model, the best fit values are  $\beta = 0.49 \pm 0.10$  and  $r_c = 3.4 \pm 0.3$  arcmin ( $0.72 \pm 0.07$  Mpc). The values of  $\beta$  are, within the errors, in agreement with those found by Adami et al. (2001) from a sample of nearby clusters ( $\beta_{\text{beta model}} = 1.0 \pm 0.02$  and  $\beta_{\text{cusped}} = 0.56 \pm 0.01$ ), while the values of  $r_c$  are significantly higher (the values in Adami et al. 2001, when converted to our cosmology, are  $r_c = 0.13 \pm 0.07$  Mpc for the beta model and  $r_c = 0.45 \pm 0.05$  Mpc for the cusped model). For comparison, the values for the gas profile are  $r_c = 1.2$  arcmin and  $\beta = 0.62$  (Elbaz et al. 1995). As expected from the density and isocontour maps (Fig. 10), the galaxy profile is less centrally peaked than the gas profile. The larger core radius found for the galaxies reflects the elongated, bimodal galaxy distribution in the central region.

## 4. Velocity distribution

### 4.1. General behavior

In this section we analyze the high precision spectroscopic sample (Flag 0, 430 galaxies) and the total sample (Flags 0 and 1, 476 galaxies). A visual inspection of the raw velocity histogram (Fig. 12) clearly shows the main component of the cluster at  $\sim 60\,000$  km s<sup>-1</sup>, while background overdensities are detected at  $\sim 74\,000$  km s<sup>-1</sup> (18 objects), and more marginally at  $\sim 90\,000$  km s<sup>-1</sup> (11 objects). In the wide field image (Fig. 2), the galaxies in the velocity bins corresponding to these three peaks are marked with different symbols.

A critical point is the identification of cluster members and the exclusion of interlopers (see e.g. den Hartog & Katgert 1996). As A 2163 is a rich cluster, we must take into account its broad velocity distribution. Within  $\pm 6000$  km s<sup>-1</sup> from the main peak of the velocity distribution at  $\sim 60\,000$  km s<sup>-1</sup>, we

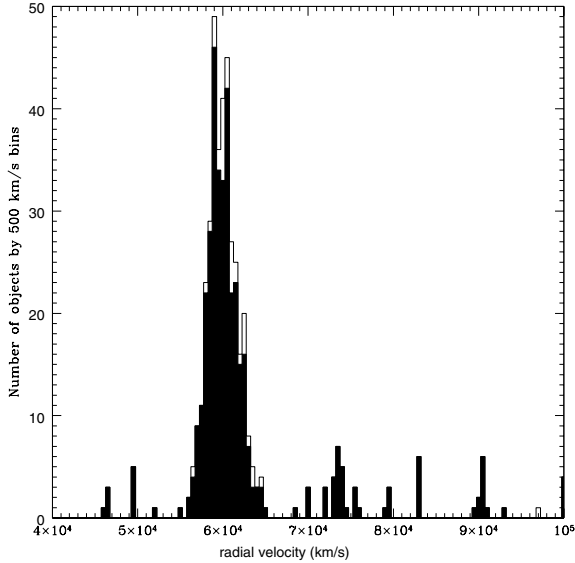


**Fig. 12.** Velocity distribution histogram in the WFI field centered on A 2163. Filled histogram: high precision VIMOS spectroscopic catalog (430 galaxies). Empty histogram: total sample including redshifts from CFHT spectra and low S/N VIMOS spectra (476 galaxies).

find 326 galaxies from the high precision (Flag 0) catalog. This sample satisfies the criterion of a maximum velocity gap of  $1000 \text{ km s}^{-1}$  between adjacent members in velocity space. An alternative way to select cluster members is the classical three-sigma clipping method (Yahil & Vidal 1977). We have applied this to all Flag 0 galaxies within the redshift range  $0.18 \leq z \leq 0.22$ , obtaining the same final sample of 326 galaxies. We have also checked the velocity of these galaxies as a function of their projected distance from the cluster center, finding no significant outliers. Applying the same analysis to the total (flag 0+1) sample, we find 361 cluster members. These are our reference redshift-selected catalogs of cluster members, which were used to study the kinematical and dynamical properties of A 2163.

Applying the program ROSTAT (Beers et al. 1990), we find very stable values for the cluster mean velocity and velocity dispersion calculated with the different methods. In Table 4 we give the biweight estimates of the location  $C_{\text{BI}}$  and scale  $S_{\text{BI}}$ , which are better estimators than the classical mean and standard deviation, for different subsamples. The total cluster sample with 361 galaxies and the high-precision sample with 326 galaxies have comparable values of location and scale, and each give an exceptionally large value for the velocity dispersion ( $\sim 1430 \text{ km s}^{-1}$ ). The subsample including only emission line galaxies shows – not surprisingly – a higher velocity dispersion, with a value of  $1564^{+152}_{-152} \text{ km s}^{-1}$ ; its mean velocity is marginally higher than the mean velocity of the no emission and total cluster samples, with a velocity offset  $\Delta V = 400 \pm 280 \text{ km s}^{-1}$ . The velocity distribution of these objects (see Fig. 13) is very broad. Their projected spatial distribution (Fig. 6) shows that most of them lie in the cluster outskirts. These results are expected for late-type galaxies infalling on the main cluster. However, several emission line galaxies are found within the cluster core, which is quite unusual. We have examined in more detail the position of the emission line galaxies in the field, by dividing the  $30' \times 30'$  field in individual cells of  $10' \times 10'$ , and estimating the fraction of emission line cluster members in each cell. The mean fraction in the whole field is  $\sim 13\%$ . There is a systematic increase of the fraction from the central cell, where it has the minimum value of  $\sim 6.5\%$ , to the lateral cells where the mean value is  $\sim 11\%$ .

However, in the western region of the cluster it reaches the high value of  $\sim 30\%$ . This corresponds to the excess shown in Fig. 6 in the immediate surroundings of A 2163-D.

When excluding emission line galaxies, the cluster velocity dispersion decreases slightly but retains a high value:  $1403^{+63}_{-63} \text{ km s}^{-1}$ . However, our estimate could be affected by substructures. For example, a visual inspection of the histogram in Fig. 13 shows bimodality in the central part of the velocity distribution, with two peaks at  $\sim 59000 \text{ km s}^{-1}$  and  $\sim 60500 \text{ km s}^{-1}$ ; it also suggests a lack of galaxies (with respect to the Gaussian fit) at  $\sim 61000 \text{ km s}^{-1}$ , and the presence of a third peak at  $\sim 63000 \text{ km s}^{-1}$ . It is not clear how real these deviations from a Gaussian distribution are, or whether they are artifacts of sampling. In the following section we address the details of the velocity distribution of the cluster with the appropriate statistical tools.

The velocity histogram suggests the presence of a background structure at  $\sim 74000 \text{ km s}^{-1}$ . Selecting all galaxies between  $71000 \text{ km s}^{-1}$  and  $77000 \text{ km s}^{-1}$  (18 objects, marked with blue triangles in Fig. 2), and applying ROSTAT, we find  $C_{\text{BI}} = 73724 \pm 182 \text{ km s}^{-1}$  and  $S_{\text{BI}} = 848^{+243}_{-242} \text{ km s}^{-1}$ . These values would be consistent with a background cluster seen on the same line-of-sight as A 2163, but no significant concentration is seen in the projected distribution of the 18 galaxies (see Fig. 2). Moreover, most of these galaxies (13 of 18) show emission lines. These facts suggest that the background overdensity is probably due to field galaxies within a large-scale structure and is not due to a cluster: there may be a large scale filament spreading from the SE to the NW of the field.

Finally, there is another small peak in the velocity histogram at  $\sim 90000 \text{ km s}^{-1}$ , for which we have 11 redshifts. As in the previous case, the projected distribution of these galaxies (green diamonds in Fig. 2) does not show any significant density concentration. The objects seem to populate a strip crossing the field along the N–S direction, and half of them present emission lines, again suggesting a population of field galaxies. More redshifts would be necessary to identify any possible structures.

#### 4.2. Statistical analysis of the velocity distribution

In order to characterize the dynamical state of A 2163, we performed quantitative tests which check if the velocity distribution can be reproduced by one or more Gaussian functions, applying them to the high precision spectroscopic sample (326 objects). Among the 15 normality tests of the ROSTAT program (Beers et al. 1990), only two (the B2 and KS tests) reject the Gaussian hypothesis at a significance level  $\leq 10\%$ .

We also used two types of shape estimators: the traditional third and fourth moments, i.e. skewness and kurtosis, and the asymmetry and tail indices (Bird & Beers 1993) in order to test the null hypothesis of a Gaussian velocity distribution. None of them shows strong deviation from a Gaussian velocity distribution, with the exception of a slight indication of positive (i.e. above the mean velocity) asymmetry in the whole sample given by the skewness parameter. An indication of a possible deviation from Gaussianity is the presence of gaps in the observed velocity distribution (Beers et al. 1991). We detected five significant weighted gaps; two of them are close to the mean radial velocity of the cluster ( $60131 \text{ km s}^{-1}$ ).

In order to quantify the deviation of the velocity distribution from a single Gaussian, we have applied the Ashman et al. (1994) implementation of Kaye’s Mixture Model algorithm (KMM, McLachlan & Basford 1988). This algorithm fits a given number of Gaussian distributions to the data, calculating the maximum likelihood values for the mean and the

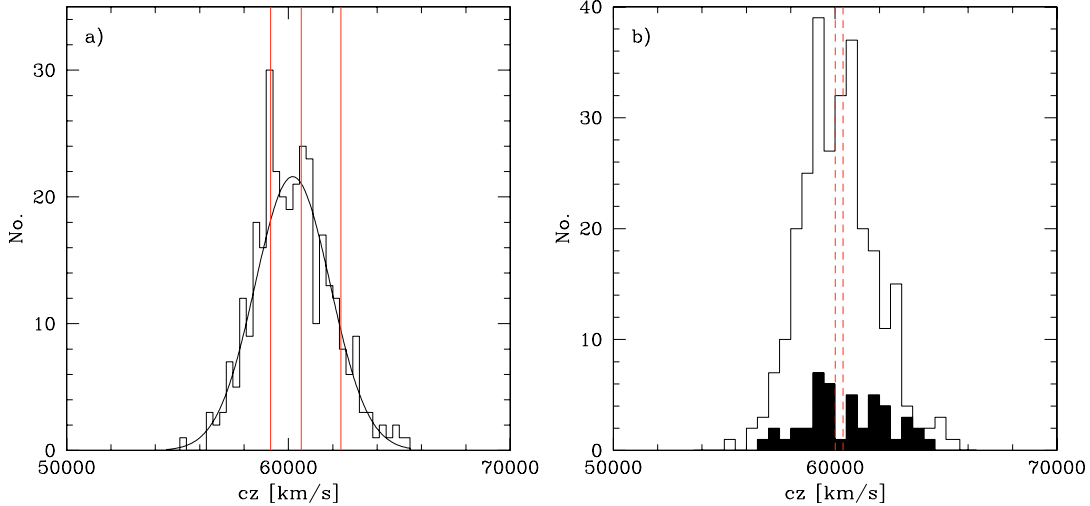


**Fig. 13. a)** Velocity histogram of the confirmed cluster galaxies in our high precision redshift sample (326 members), with the Gaussian best-fit. Bins of  $300 \text{ km s}^{-1}$  have been used. The thick solid lines correspond to the estimated mean velocities of the three groups identified by KMM. **b)** Same sample as in **a)**, but divided into galaxies without emission lines (empty histogram), and with emission lines (filled histogram). Bins of  $500 \text{ km s}^{-1}$  have been used. The velocities of the two BCGs are plotted as red dashed lines.

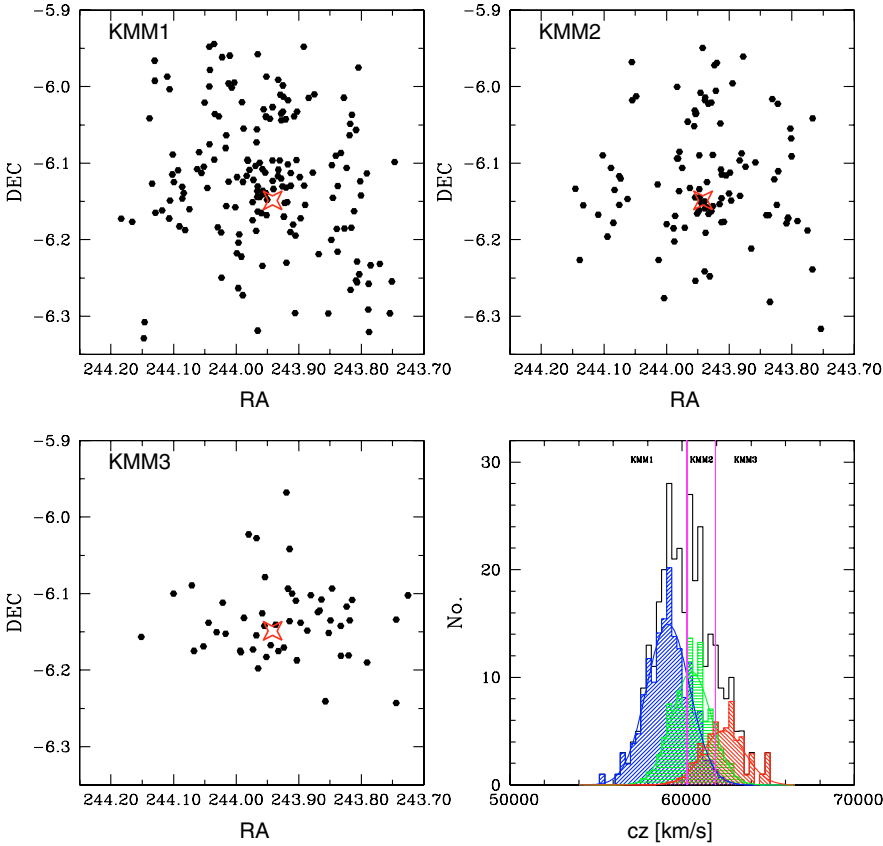


**Fig. 14.** Projected distribution of galaxies and velocity histograms ( $300 \text{ km s}^{-1}$  bins) for the three KMM partitions of A 2163. The open star indicates the peak of the X-ray emission. The bottom right panel shows the global velocity histogram (in black) and the expected histograms for KMM1 (blue) KMM2 (green) and KMM3 (red) with their respective Gaussian fits. The two magenta vertical lines represent the velocity limits  $V_1$  and  $V_2$  of the three partitions. Galaxies with velocity  $< V_1$  are associated with KMM1; galaxies with velocity  $> V_2$  are associated with KMM3; galaxies in the intermediate range are associated with KMM2 (see text).

variance, and evaluating the improvement with respect to a single Gaussian fit. In particular, it gives as output the  $P$ -value, which is the probability of measuring the observed value of the likelihood ratio test statistic for a sample drawn from a single Gaussian parent population: the null hypothesis of a single Gaussian parent population is conventionally rejected if  $P < 0.05$  and is marginally inconsistent if  $0.05 < P < 0.1$ . On the basis of the above results, we have tried to fit two and three Gaussian components to our data. In both cases, the KMM does not reject the null hypothesis. For example, the two-component fit identifies the

first group at a mean velocity of  $59517 \text{ km s}^{-1}$  and the second one at  $61729 \text{ km s}^{-1}$ , with a  $P$ -value of 0.17, assuming the homoskedastic case, i.e. the same velocity dispersion for the different components. Moreover, the two-Gaussian fit fails to detect the peak at  $\sim 60500 \text{ km s}^{-1}$ . This is not surprising, as the velocity separation between the first two peaks is comparable to the velocity dispersion of the groups (theoretically two equal Gaussian distributions can be separated if their peaks have a separation  $\geq 2\sigma$ , Everitt & Hand 1981). However, when applying a three-component Gaussian fit to the data (assuming as first guesses the peaks at  $59000 \text{ km s}^{-1}$ ,  $60500 \text{ km s}^{-1}$

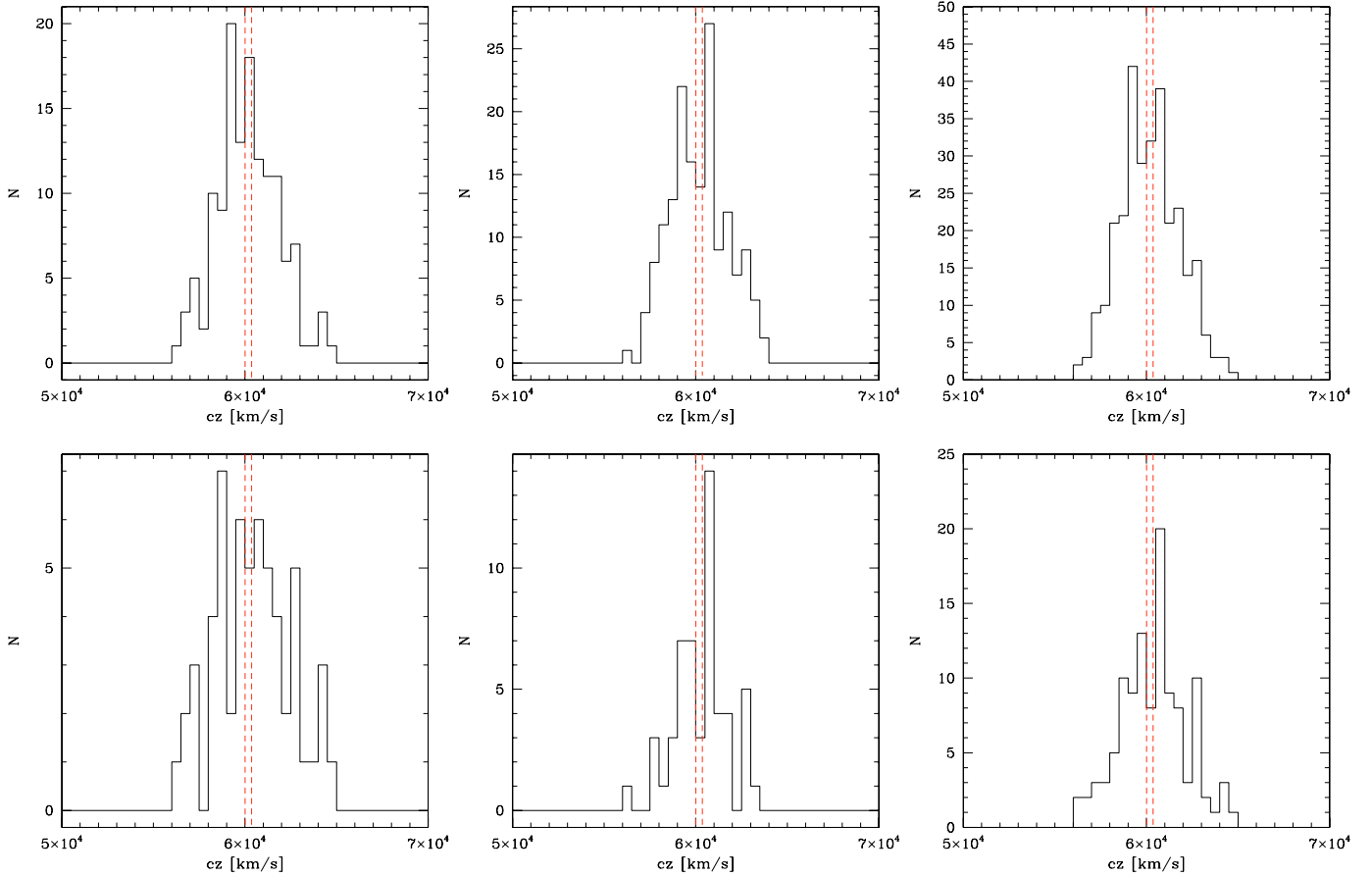


**Fig. 15.** Velocity histograms as functions of luminosity and field size. *Top row:* whole field; *bottom row:* circular region within a 5 arcmin radius centered on A 2163-A. *Left column:* “bright” ( $R \leq 19$ ) galaxies; *central column:* “faint” ( $19 < R \leq 21$ ) galaxies; *right column:* the whole magnitude range  $R \leq 21$ . The velocities of the two BCGs are plotted as red dashed lines.

and  $63\,000\text{ km s}^{-1}$ ), the KMM identifies the two central peaks around the mean cluster velocity, with a third component at  $\sim 62\,400\text{ km s}^{-1}$  (see Table 4). While these groups are not statistically significant in the velocity space, we use the KMM results with three Gaussians as an objective method to partition the data and as a starting point for the following combined analysis, which makes use of the projected positions.

The mean velocities of the three fitted groups are shown with thick lines in the left panel of Fig. 13, and the velocity distribution properties of the three partitions are listed in Table 4 (notice that the relative richness of the KMM groups is not very robust; for example, in the homoskedastic case, i.e. imposing the same velocity dispersion for the three components, KMM2 becomes the richest). The two main partitions KMM1 and KMM2 correspond to the central peaks in the velocity histogram and have an offset in velocity of  $\sim 1360\text{ km s}^{-1}$  (corresponding to a physical  $\Delta V \sim 1130\text{ km s}^{-1}$  in the reference system of the cluster), while KMM3 includes the  $63\,000\text{ km s}^{-1}$  peak but is not centered on it.

The velocity and spatial distributions of the three KMM partitions are shown in Fig. 14. For each galaxy, the KMM algorithm estimates the probability of belonging to each partition, associating the galaxy to the partition with the highest probability. As a result, all galaxies below a “critical” velocity  $V_1$  are associated to KMM1, all galaxies above a critical velocity  $V_2$  are associated to KMM3, and those between  $V_1$  and  $V_2$  are associated to KMM2. In order to reconstruct the velocity distributions without artificial cutoffs, for each partition we have summed up

the corresponding probabilities of all the galaxies in each velocity bin. The fourth panel of Fig. 14 shows  $V_1$  and  $V_2$  as vertical lines and the reconstructed velocity distributions of the three partitions with the corresponding Gaussian fits.

From the projected distribution of the galaxies displayed in the first three panels of Fig. 14, an offset is apparent along the NE/SW direction between the spatial distributions of the two main velocity partitions. KMM1 objects are more concentrated towards the NE side of the peak of X-ray emission, while KMM2 objects show a more clumpy distribution, the main concentration being located more towards the central-SW region of the cluster compared to KMM1 galaxies. Applying the Kolmogorov-Smirnov test indicates that the probability that the two distributions are issued from the same parent distributions is excluded at more than 99% confidence level. A more detailed comparison of the spatial distributions of KMM1 and KMM2 objects will be addressed in Sect. 5.2. Galaxies in the KMM3 partition are more concentrated towards the central region of the cluster, tracing the elongation in the EW direction. This could be due to projection effects, since infalling field galaxies, characterized by radial orbits towards the cluster center, have a higher radial component to their proper velocity when observed in projection at the cluster center. Indeed galaxies in the lower tail of the velocity distribution of A 2163 show a very similar spatial distribution. Nevertheless, we cannot exclude that the small excess of galaxies in KMM3 is a group at a higher radial velocity with respect to the cluster mean.

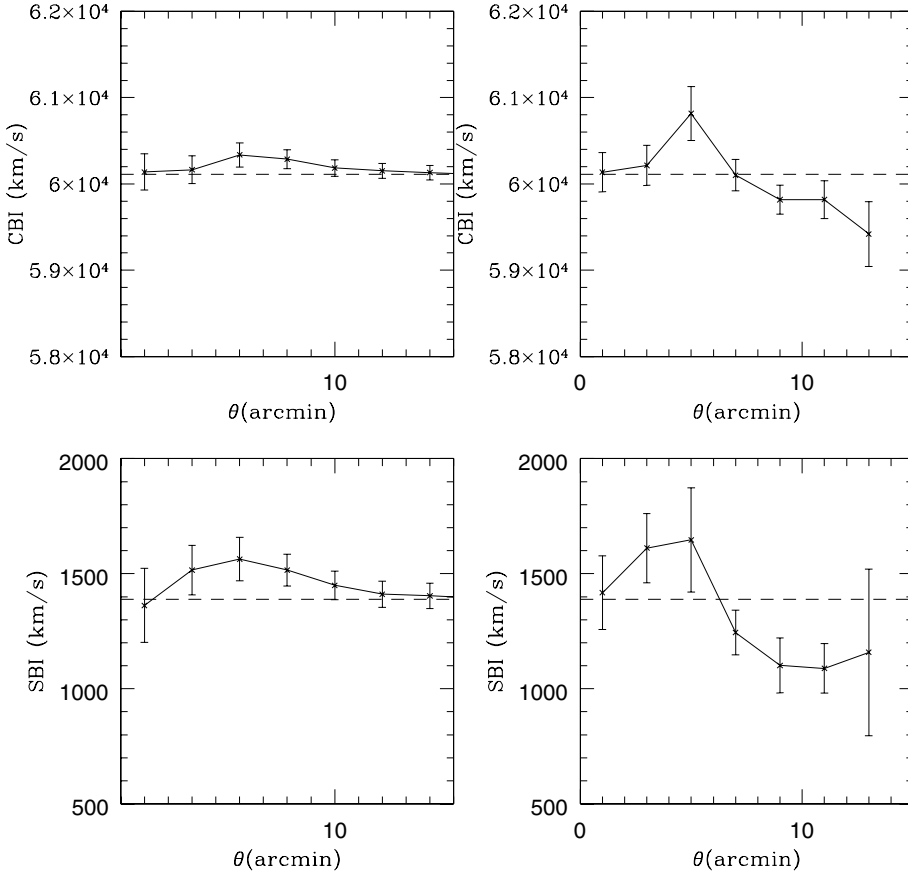


**Fig. 16.** Mean velocity (*top*) and velocity dispersion (*bottom*) profiles. The plots on the left correspond to integrated profiles, while those on the right to differential profiles. The error bars correspond to  $1\sigma$  errors calculated from 10 000 bootstrap catalogs. Horizontal short-dashed lines mark the estimated values of the mean velocity and velocity dispersion, respectively, for the whole sample.

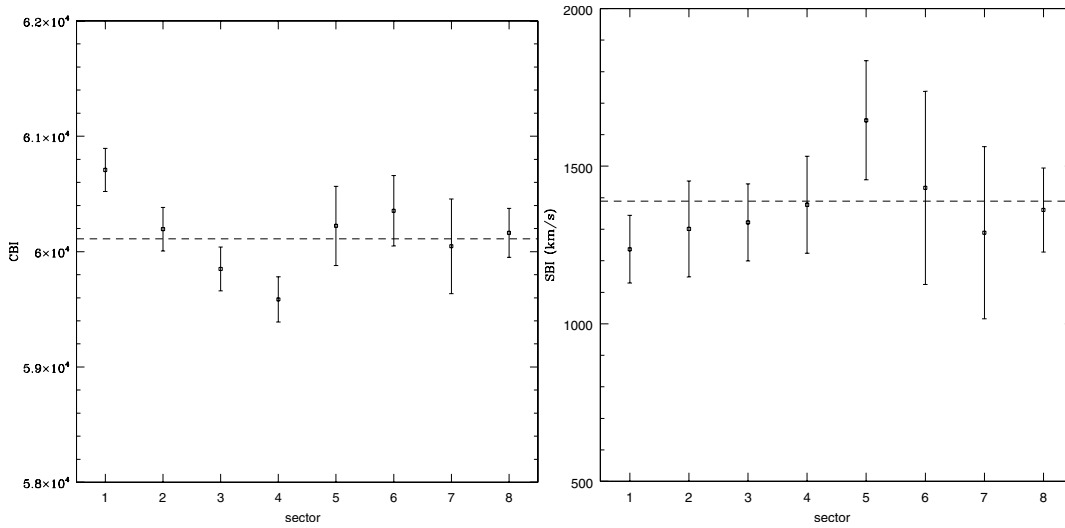


**Fig. 17.** Mean velocity (*left*) and velocity dispersion (*right*) estimated in 45 degree sectors. These are labeled from 1 to 8 anti-clockwise. In this notation, sector 1 corresponds to 0–45 degrees, sector 2 to 45–90 degrees, etc.

#### 4.3. Velocity distribution as a function of luminosity

We have discussed the variation of the projected density distribution of galaxies as a function of galaxy luminosity in the central component A 2163-A. Here we will investigate the dependence of the velocity distribution on the galaxy luminosity. For this purpose, we have divided our high quality cluster spectroscopic sample in two luminosity classes, bright ( $R \leq 19$ , 137 galaxies), and faint ( $19 \leq R \leq 21$ , 161 galaxies), and we have analyzed the two subsamples with ROSTAT. Their velocity distributions are shown in Fig. 15 and the values of location and scale are listed

in Table 4. A similar analysis was performed in the central region of the cluster, corresponding to A 2163-A, within a radius of 5 arcmin from the X-ray center.

Concerning the  $30' \times 30'$  field, the estimates of location for the two luminosity classes are consistent and are in good agreement with the estimate for the whole sample. The velocity dispersion of the bright sample is  $\sim 90 \text{ km s}^{-1}$  higher than that of the total sample, while the velocity dispersion of the faint sample is  $\sim 80 \text{ km s}^{-1}$  lower than that of the total sample, but at only the  $1\sigma$  level. The histograms (Fig. 15) show that the bimodality previously detected around  $60\,000 \text{ km s}^{-1}$  for the whole sample is still

**Table 4.**  $C_{\text{BI}}$  and  $S_{\text{BI}}$ , the biweight estimators for location and scale and the associated errors computed with ROSTAT (Beers et al. 1990) for different subsamples, with the exception of the KMM partitions (see Sect. 4.2), for which we give the standard mean velocity and velocity dispersion and the corresponding bootstrap errors.

Field	Population	Flag	$R$ [km s <sup>-1</sup> ]	$C_{\text{BI}}$ [km s <sup>-1</sup> ]	$S_{\text{BI}}$	$N_{\text{gal}}$
30' × 30'	all	0+1	$R < 22$	60217 <sup>+82</sup> <sub>-82</sub>	1437 <sup>+56</sup> <sub>-56</sub>	361
30' × 30'	all	0	$R < 22$	60131 <sup>+86</sup> <sub>-86</sub>	1434 <sup>+59</sup> <sub>-59</sub>	326
30' × 30'	no emission	0	$R < 22$	60080 <sup>+89</sup> <sub>-89</sub>	1409 <sup>+63</sup> <sub>-63</sub>	284
30' × 30'	only emission	0	$R < 22$	60491 <sup>+266</sup> <sub>-266</sub>	1564 <sup>+152</sup> <sub>-151</sub>	42
30' × 30'	all	0	$R < 19$	60153 <sup>+135</sup> <sub>-135</sub>	1529 <sup>+106</sup> <sub>-106</sub>	137
30' × 30'	all	0	$19 < R < 21$	60190 <sup>+115</sup> <sub>-115</sub>	1360 <sup>+69</sup> <sub>-69</sub>	161
$\theta < 5'$	all	0	$R < 22$	60386 <sup>+155</sup> <sub>-155</sub>	1636 <sup>+111</sup> <sub>-112</sub>	123
$\theta < 5'$	all	0	$R < 19$	60548 <sup>+258</sup> <sub>-258</sub>	1862 <sup>+156</sup> <sub>-156</sub>	61
$\theta < 5'$	all	0	$19 < R < 21$	60416 <sup>+169</sup> <sub>-169</sub>	1240 <sup>+141</sup> <sub>-141</sub>	54
Field	Partition	Flag	$R$ [km s <sup>-1</sup> ]	$\langle V \rangle$ [km s <sup>-1</sup> ]	$\sigma$	$N_{\text{gal}}$
30' × 30'	KMM1	0	$R < 22$	59186 <sup>+317</sup> <sub>-317</sub>	1039 ± 230	172
30' × 30'	KMM2	0	$R < 22$	60545 <sup>+484</sup> <sub>-484</sub>	951 ± 283	102
30' × 30'	KMM3	0	$R < 22$	62410 <sup>+292</sup> <sub>-292</sub>	1016 ± 212	52

present for both the bright and faint subsamples. Faint galaxies appear to be slightly more numerous in the  $\sim 60\,500$  km s<sup>-1</sup> peak.

Restricting the analysis to the inner 5 arcmin field (bottom row in Fig. 15), we find that the estimates of location for the two luminosity classes are stable and consistent, with a value  $\sim 200$  km s<sup>-1</sup> higher than the estimate for the whole field but still consistent taking into account the large error bars. On the other hand, as in the case of the 30' × 30' field, the velocity dispersion of the faint sample ( $1239 \pm 141$  km s<sup>-1</sup>) is smaller than that of the bright sample ( $1862 \pm 156$  km s<sup>-1</sup>), but now the effect appears statistically significant ( $3\sigma$ ). This might indicate that the population of faint objects in the core is more relaxed. The peak at  $\sim 60\,500$  km s<sup>-1</sup> becomes more dominant when analyzing the distribution of faint objects in the core. The comparison between the velocity distribution in the core and that in the whole field suggests that the velocity peak at  $\sim 59\,000$  km s<sup>-1</sup> is mostly composed of faint and bright objects outside the inner 5 arcmin, while the one at  $\sim 60\,500$  km s<sup>-1</sup> is dominated by the faint population within the core. The third peak at  $\sim 62\,500$  km s<sup>-1</sup> is particularly apparent in the core (as it was apparent in the projected distribution of KMM3 objects shown in Fig. 14) and is composed both of faint and bright galaxies. In the following sections we present a more detailed analysis of the relative projected density distribution of these objects.

#### 4.4. Spatial variation of the velocity distribution

We have analyzed the velocity distribution in different cluster regions, addressing the variation of the global quantities, location and scale, as a function of the angular distance to the cluster center and of the position angle. We have again chosen the position of the X-ray centroid as the cluster center. For our first purpose, we have measured the location  $C_{\text{BI}}$  and scale  $S_{\text{BI}}$  in increasing circular annuli. The differential and integrated profiles of these quantities are shown in Fig. 16. The velocity profile reaches a maximum  $V \sim 60\,800$  km s<sup>-1</sup> at an angular scale of  $\sim 5$  arcmin, then declines to  $\sim 59\,400$  km s<sup>-1</sup>. While a determination of the exact profile is difficult due to the large error bars, the mean

velocity in the inner cluster region is significantly higher than in the outer region.

The velocity dispersion profile has very high values ( $\sim 1400$  to  $1600$  km s<sup>-1</sup>) in the inner region (up to  $\sim 6$  arcmin), then drops to lower values ( $1100$  km s<sup>-1</sup>) at larger scales. Here again, the error bars are large, but when comparing the value in the 2–4 arcmin bin to that in the 8–10 and 10–12 bins, the effect is  $3\sigma$  significant.

Given the complexity of the system, we analyzed the variations of the velocity distribution not only as a function of the distance to the center, but also in sectors at different position angles. We have estimated  $C_{\text{BI}}$  and  $S_{\text{BI}}$  in eight angular sectors, each one 45 degrees wide, centered on the X-ray centroid and rotating counterclockwise starting from West on the right ascension axis. These measurements are shown in Fig. 17. The mean velocity shows a systematic trend, reaching a maximum value ( $C_{\text{BI}} \sim 60\,700$  km s<sup>-1</sup>) in the 0–45 degrees sector, and a minimum nearly in the opposite direction, with values lower than the mean in the North-East quarter (90–180 degrees). The velocity dispersion is quite high in all sectors, with a particularly high value of  $S_{\text{BI}} \sim 1700$  km s<sup>-1</sup> in sector 5 (180–225 degrees). Unfortunately our sampling is not sufficient to consider this high value as statistically significant.

We conclude that there are variations of the velocity distribution between different field regions; the velocity dispersion decreases with radius, and the value of the mean velocity is lower in the NE region than in the NW (and also lower with respect to the cluster mean).

In the following we will investigate how the features of the velocity distribution are connected to the overdensities identified in the projected density distribution.

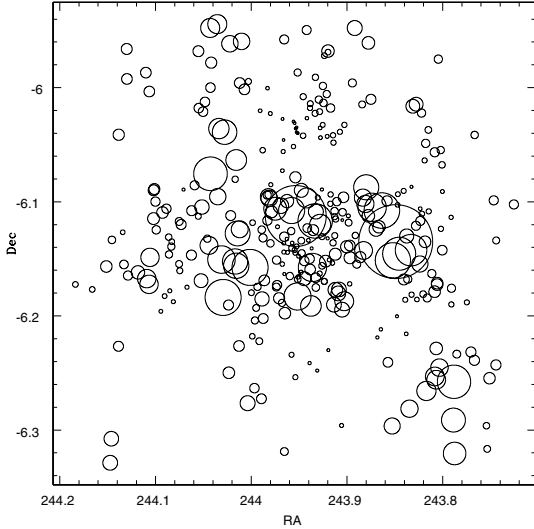
## 5. Combined velocity-density analysis of subclustering

### 5.1. Kinematical indicators of subclustering

We have applied three classical methods that quantify the amount of substructure in galaxy clusters using a combined

**Table 5.** 3D substructure indicators for the sample of 326 confirmed cluster members in our dataset.

Indicator	Value	Significance
$\Delta$	428.790	0.002
$\alpha$	$0.478 h_0^{-1}$ Mpc	0.012
$\epsilon$	$3.369 \times 10^{27}$ kg	0.999

**Fig. 18.** Projected positions of the galaxies in our spectroscopic sample, represented by circles with size weighted by the  $\delta$  estimator of Dressler & Shectman (1988). Concentrations of large circles indicate a correlated spatial and kinematic variation.

analysis of the velocity and spatial distributions of confirmed cluster members, i.e. the  $\Delta$ ,  $\alpha$  and  $\epsilon$  tests by Dressler & Shectman (1988); West & Bothun (1990) and Bird (1994) respectively. The values of the  $\Delta$ ,  $\alpha$  and  $\epsilon$  parameters and their significance levels are summarised in Table 5. Significance levels were obtained using the bootstrap technique and normalized with 1000 Monte Carlo simulations.

Assuming that these tests reject the null hypothesis for significance levels lower than 10%, both the  $\Delta$  and  $\alpha$  tests find strong evidence of subclustering, with significance levels  $\lesssim 1\%$ . Subclustering is not detected by the  $\epsilon$  test, which was shown in Pinkney et al. (1996) to be less sensitive than the  $\Delta$  and  $\alpha$  tests.

In Fig. 18 we show the results of the Dressler & Shectman (1988) test. The projected position of each galaxy is represented by a circle whose radius is weighted by the corresponding  $\delta$  parameter<sup>1</sup>. Large circles indicate local spatial and/or kinematic variations with respect to the global cluster properties, i.e. local velocity dispersion and/or mean velocity significantly different from the global cluster values. From this plot, we do not detect any strong concentration of large circles which would indicate the presence of a significant substructure. However, large circles appear to be more frequent in the northern region of A 2163-A, and west of the main cluster. Given the highly significant value of the  $\Delta$  and  $\alpha$  tests and the local concentrations of circles, we investigate below the correlation of subclustering in velocity and density space in more detail.

## 5.2. Slicing the density distribution in velocity and luminosity space

As shown in Sects. 4.3 and 4.4, we have detected several signatures indicating that the velocity distribution depends on the luminosity and on the spatial location of galaxies. Here we investigate the relationship between the substructures visible in the projected density distribution and the partitions detected in the velocity distribution, testing the dependence of the projected density both on the velocity and on the luminosity range. For this purpose, we have built several sets of galaxy density maps using those galaxies with a measured redshift (spectroscopic sample).

In Fig. 19 we show the density maps for all the galaxies which are members of the cluster and for the galaxies associated to the KMM1 and KMM2 partitions (Sect. 4.2). We omit KMM3 as its number of objects is too small; these objects were shown to be located preferentially in the central region corresponding to A 2163-A. We have furthermore selected galaxies in three magnitude ranges, applying the same criteria as in Sect. 4.3: the whole magnitude range ( $R < 21$ ), and the bright ( $R \leq 19$ ) and faint ( $19 < R \leq 21$ ) ranges. In each case, we overplot the isocontours of the projected density distribution for the *photometric* sample corresponding to the same magnitude limits, as it does not suffer of the sampling inhomogeneities of the spectroscopic sample. We stress that the spectroscopic sampling is homogeneous only in the central field and for the bright galaxies ( $R \leq 19$ ): for this reason the density maps of fainter galaxies are biased and require a careful interpretation.

We have also built density maps for galaxies in different velocity ranges. In the case of the bright subsample ( $R < 19$ , top row), the density map of all the confirmed velocity members of the cluster (top left) is in very good agreement with the projected density map of the photometric catalogue at the same magnitude limit. Both subclusters A 2163-A and A 2163-B are clearly visible on the map (and to some extent A 2163-C, which is however in a region not very well sampled by spectroscopy). In the main cluster A 2163-A, the NE/SW orientation is confirmed, and the deformations of the projected isocontours in its periphery are shown to be due to the presence of small groups belonging to the cluster. The density maps of galaxies in the KMM1 and KMM2 partitions (top middle and top right) reveal some differences. While KMM2 follows the projected high density structure with maxima A1 and A2, KMM1 is clearly located in the northern region of A 2163-A. This is in good agreement with the previous analysis of the velocity distribution in sectors, which showed a lower mean velocity in the NE sectors (Fig. 17).

The density maps of faint galaxies ( $19 < R \leq 21$ , middle line) in KMM1 (central panel) and KMM2 (middle row, right column) indicate clear differences. The same is observed when considering all galaxies with  $R \leq 21$ . Looking at A 2163-A, there is an offset in the core along the NE/SW axis between the projected density maxima of KMM1 and KMM2, consistent with Fig. 14. In the density maps of the spectroscopic sample there are no clear peaks corresponding to the A2, D and E components, although they are apparent in the density maps of the photometric catalogue: this is due to the low spectroscopic sampling rate in those regions.

For the whole velocity range within the cluster (left column), when varying the magnitude range from bright to faint galaxies (top left to middle left panels), there is a shift of the main peak within the core of A 2163-A along the N-NE/S-SW axis. The positions of the density maxima for both KMM1 and KMM2 (middle and right columns) show also variations with luminosity. We conclude that the galaxies associated with different velocity

<sup>1</sup> The Dressler & Shectman (1988) test associates a  $\delta$  value to each galaxy,  $\Delta$  being the sum of all  $\delta$ .

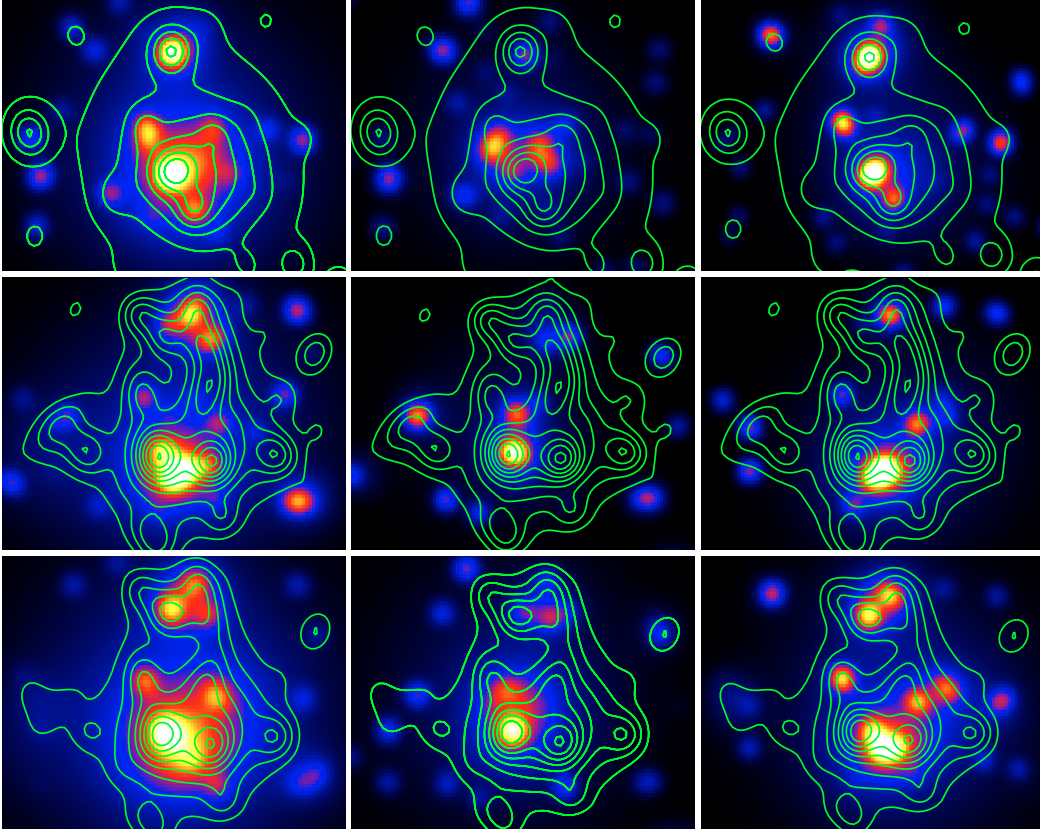


**Fig. 19.** Density maps of A 2163 in velocity and luminosity space, derived from the spectroscopic sample. Rows correspond to different magnitude limits:  $R < 19$  bright subsample (*top*),  $19 < R < 21$  faint subsample (*middle*),  $R < 21$  total sample (*bottom*). Columns correspond to different velocity limits: all spectroscopically confirmed cluster members (*left*), members of the KMM1 partition (*middle*), members of the KMM2 partition (*right*). Projected density maps of the photometric sample as discussed in Sect. 3, corresponding to galaxies with  $R < 19$  (*top*), and to galaxies with  $19 < R < 21$  (*middle*), and to  $R < 21$  (*bottom*), are denoted by the superimposed contours.

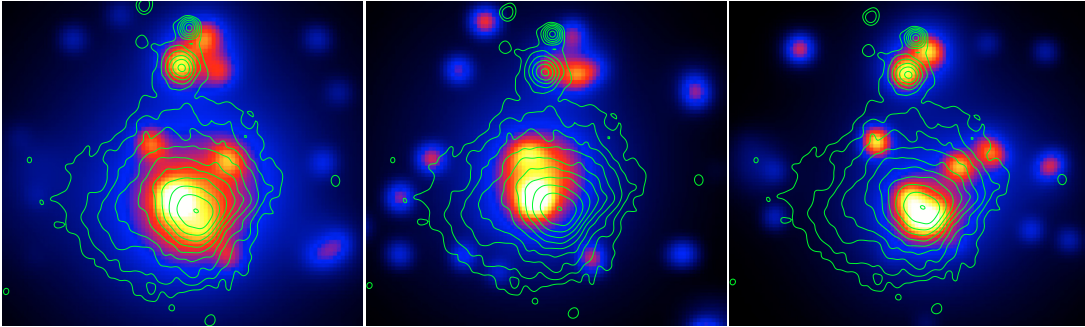


**Fig. 20.** Density maps of A 2163 in velocity space for galaxies with  $R < 21$  (the same as in the *bottom* row in Fig. 19) with superimposed X-ray isocontours. *Left panel:* all galaxies with a measured redshift; *middle panel:* galaxies associated to the KMM1 partition; *right panel:* galaxies associated to the KMM2 partition. X-ray contours have a logarithmic step of 0.2 dex, with the lowest contour at  $4.65\text{E-}3$  ct/s/arcmin<sup>2</sup> and the highest at  $1.86\text{E-}1$  ct/s/arcmin<sup>2</sup>.

partitions have different projected density distributions, and this is true whatever be their luminosity range. Moreover, the projected density distributions of all the velocity partitions vary systematically with the luminosity range.

In Fig. 20 we compare the density maps of the spectroscopic sample including the whole magnitude range ( $R < 21$ ) to the X-ray isocontours. The X-ray maximum of the main component A 2163-A is located between the density peaks corresponding to KMM1 and KMM2, lying very close to the KMM2 peak. KMM1 is clearly offset to the NE with respect to the X-ray

contours. More strikingly, the compressed X-ray contours in the SW region are roughly perpendicular to the axis joining KMM1 and KMM2.

### 5.3. The peripheral subclusters

The projected galaxy density distribution (Fig. 5) has shown the presence of two particularly significant subclusters, North and East of the main component (A 2163-B and A 2163-C), and of smaller clumps, West (A 2163-D) and South (A 2163-E)

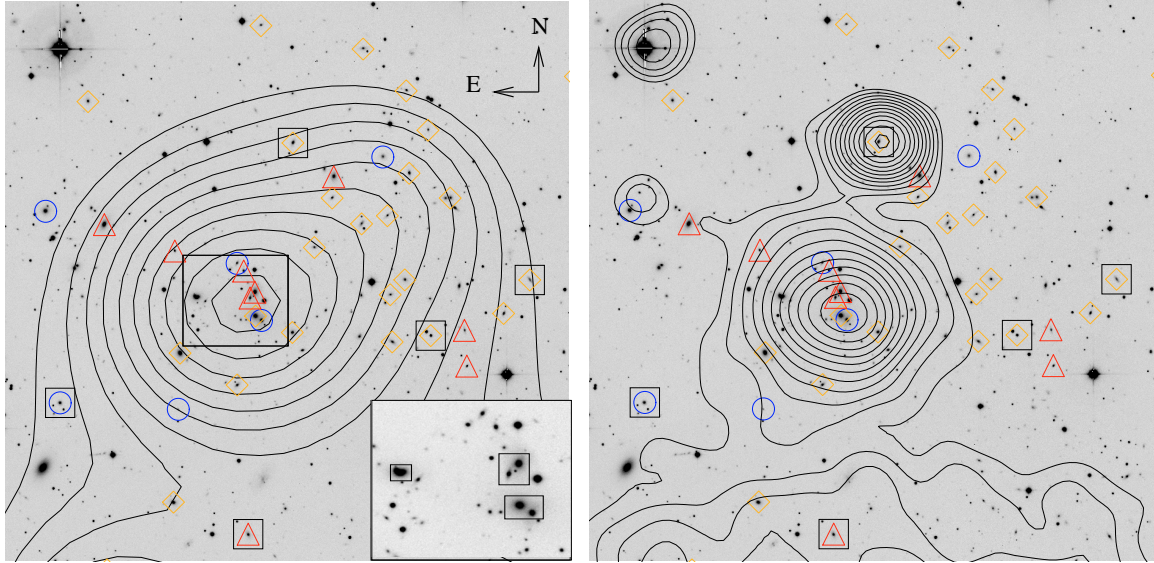


**Fig. 21.** A close-up view on a  $6' \times 6'$  region centered on A 2163B (northern group). (*Left*) The projected galaxy density contours ( $R \leq 19.5$ ) are superimposed on the  $R$ -band WFI image. Galaxies with measured redshifts are separated into three velocity intervals, corresponding to the three peaks in the velocity histogram. Blue circles correspond to the range  $[57\,000\text{--}59\,000]$   $\text{km s}^{-1}$ , yellow diamonds to  $[59\,000\text{--}61\,000]$   $\text{km s}^{-1}$  and red triangles to  $[61\,000\text{--}63\,000]$   $\text{km s}^{-1}$ . Black squares identify galaxies with emission lines. A zoom on the central region of the subcluster is shown in the bottom right corner, where rectangles identify the northern pair, the southern pair and the dumbbell galaxy. (*Right*) The same with the projected X-ray contours from XMM.

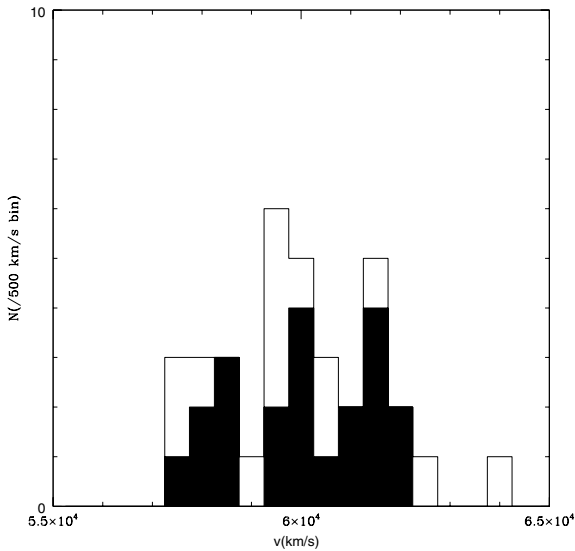


**Fig. 22.** Velocity histogram of A 2163B (northern group). Open and filled histograms include galaxies within 3 and 2 arcmin, respectively from the density maximum.

respectively. We have used our spectroscopic data to establish if these components belong to the A 2163 complex. Unfortunately the regions of A 2163-D and A 2163-E are sparsely sampled. In the case of A 2163-C, 15 redshifts are available within a radius of 2 arcmin from its center: the mean location is  $C_{\text{BI}} = 59\,960$   $\text{km s}^{-1}$ , thus confirming its association to the A 2163 complex.

In Fig. 21 we show the projected density distribution of galaxies in A 2163-B ( $R \leq 19.5$ ), which is centered on a dense group of bright objects with two galaxy pairs. Contours are roughly elliptical in the center and progressively elongated along a tail extending North-West. This tail becomes more prominent

and extended when including fainter magnitudes (see Fig. 19, left panel).

The right panel of Fig. 21 shows the X-ray contours from XMM data superimposed on the  $R$ -band image. A secondary peak in the X-ray emission, North of A 2163B, is due to a galaxy which is a cluster member: it is a type 1 AGN, and its optical spectrum is shown in Fig. 1. The velocity histograms of galaxies within projected separations of 2 arcmin and 3 arcmin, respectively, from the position of the main density maximum of A 2163-B are shown in Fig. 22. Values of location and scale have been calculated with ROSTAT, leading to  $C_{\text{BI}} = 60\,272$   $\text{km s}^{-1}$  and  $S_{\text{BI}} = 1\,223$   $\text{km s}^{-1}$  (2 arcmin, 22 galaxies) and  $C_{\text{BI}} = 60\,190$   $\text{km s}^{-1}$  and  $S_{\text{BI}} = 1\,323$   $\text{km s}^{-1}$  (3 arcmin, 35 galaxies). The value of the mean velocity is in good agreement with the global one for the whole cluster (Table 4). However the velocity dispersion is high, typical of a rich cluster and not of a group.

The mean velocity of A 2163-B confirms that it is member of the same complex as A 2163-A, as indicated by the density map of galaxies within the cluster redshift range displayed in Fig. 19 (bottom left). However, the velocity distribution is complex, with three peaks at different velocities. One difficulty, due to the small angular separation of the two components (7 arcmin), is to disentangle the contribution of A 2163-B from that of the main underlying cluster A 2163-A. In order to better understand the spatial location of the galaxies belonging to the different velocity peaks, in Fig. 21 (left) we have marked them with different symbols according to the velocity range. A significant component of galaxies belonging to the intermediate velocity peak ( $\sim 60\,000$   $\text{km s}^{-1}$ ) extends all over A 2163-B, including the central elliptical galaxy on which the X-ray contours are centered (Fig. 21, right). This suggests that A 2163-A and A 2163-B have approximately the same redshift. However, both low and high velocity components are present, and strongly contribute to the measured high velocity dispersion. There is no BCG in the center of A 2163-B but there are a couple of galaxy pairs and a dumb-bell galaxy. The two galaxies of the northern pair lie at  $61\,804$   $\text{km s}^{-1}$  (for the brightest) and  $61\,920$   $\text{km s}^{-1}$ ,

revealing a “physical” pair at high velocity as compared to the main cluster. However, the two galaxies of the southern pair (a bright elliptical on which are centered the X-ray contours and a smaller object) show very different velocities ( $59\,914\text{ km s}^{-1}$  and  $58\,192\text{ km s}^{-1}$ ), implying that their pair-like aspect probably results from a projection effect. Unfortunately, the Eastern region of A 2163-B is poorly sampled. In particular, there is a concentration of galaxies around a bright dumb-bell galaxy whose redshift is unknown. With the present incomplete velocity sampling of A 2163-B, it is difficult to separate its velocity distribution from that of the main cluster. Present evidence might suggest a complex dynamical state for A 2163-B with the presence of several components in velocity space, but the low spectroscopic sampling does not allow us to reach a definitive conclusion. The relation of A 2163-B to the main complex will be further discussed in Sect. 7.

## 6. The mass of A 2163

It is well known that estimating the mass of a merging system is a difficult problem, as the general assumption on which mass calculation is based is that the system is at equilibrium (the virial theorem for optical analysis, and hydrostatic equilibrium for X-ray). However, the simple presence of substructures in a system does not automatically imply that such an estimate is unreliable: the crucial point is how far the system is from equilibrium.

In the case of A 2163, we have shown that clear signs of merging are present; on the other hand, the general regularity of its density and velocity profiles suggests that the system is not too far from equilibrium. In fact, the projected galaxy distribution of the main cluster is reasonably regular when smoothed on a sufficiently large scale. Moreover the velocity distribution, in spite of the existing bimodality, is well fitted by a Gaussian distribution. Finally, there is an excellent agreement between the X-ray temperature of the cluster ( $T = 12.4\text{ keV}$ , see Govoni et al. 2004; Pratt et al. 2001) and its global velocity dispersion: using for example the relation  $\sigma(\text{km s}^{-1}) = 10^{2.52}(kT)^{0.6}$  (Lubin & Bahcall 1993) we obtain  $\sigma = 1490\text{ km s}^{-1}$ , to be compared to our estimate of  $\sigma \approx 1400\text{ km s}^{-1}$ . There are also mass estimates from weak lensing, which do not rely on hydrostatic equilibrium, virialization or the symmetry of the system. Unfortunately, the two weak lensing velocity dispersions presently available for A 2163 are quite uncertain: for a singular isothermal model Squires et al. (1997) find  $\sigma_{\text{SIS}} = 740\text{ km s}^{-1}$ , but note that a value of  $1000\text{ km s}^{-1}$  would still be consistent with observations; with the same model, Cypriano et al. (2004) find  $\sigma_{\text{SIS}} = 1021 \pm 146\text{ km s}^{-1}$ . These values correspond to mass estimates systematically lower than that calculated from X-ray approaches. Squires et al. (1997) note that the mass estimate can be biased downwards if the cluster extends to the control annulus, and applying a tentative correction based on the X-ray derived mass profile they obtain consistent X-ray and weak lensing mass estimates. However, up to now weak lensing analysis have been restricted to relatively small, central fields ( $7' \times 7'$ ), while the cluster clearly extends at least to angular separations of  $10'$  (see Fig. 11). A weak lensing analysis using our multi-band wide-field imaging of A 2163 is in progress (Soucail et al., in prep.). Another alternative, when the merging clusters are well defined, is to estimate the mass for each clump separately and add the two components. This is not possible here, as there is too much spatial overlap between the two main velocity components identified as KMM1 and KMM2.

We have applied a standard approach to estimate the virial mass from spectroscopic and photometric data (see e.g. Ferrari et al. 2005). Under the usual assumption of spherical symmetry we have  $r_{\text{vir}} = (\pi/2)R_{\text{vir}}$ , where  $r_{\text{vir}}$  and  $R_{\text{vir}}$  are respectively the spatial and projected virial radii (see Limber & Mathews 1960), and  $\sigma_{\text{vir}} = 3\sigma_r$ , where  $\sigma_{\text{vir}}$  is the spatial virial velocity dispersion and  $\sigma_r$  is the radial velocity dispersion of the system. The virial mass  $M_{\text{vir}}$  is then:

$$M_{\text{vir}} = \frac{3}{2} \frac{\pi}{G} R_{\text{vir}} \sigma_r^2 \quad (2)$$

$R_{\text{vir}}$  is given by:

$$R_{\text{vir}} = \frac{2N}{N-1} R_h \quad (3)$$

where  $R_h$  is the projected harmonic radius

$$R_h = \frac{N(N-1)}{2} \left( \sum_{i<j}^{N-1} \sum_{j=i+1}^N \frac{1}{R_{ij}} \right)^{-1} \quad (4)$$

$R_{ij}$  is the projected separation between the  $i$ th and  $j$ th galaxies, and  $N$  is the total number of objects in the system.

For the estimate of the harmonic radius we apply the ring-wise estimator (Carlberg et al. 1996). As in Ferrari et al. (2005), we have estimated the harmonic radius selecting from our photometric catalogue the galaxies belonging to the red sequence. Using the photometric catalog we are able to have an homogeneous field coverage, and the red sequence guarantees that we are selecting early-type cluster members, excluding interlopers and therefore optimizing the mass estimate (see Biviano et al. 2006).

From our photometric catalogue we have selected all galaxies with  $16.5 \leq R \leq 20$  which belong to the red sequence, and are within 10 arcmin of the cluster center (corresponding to 2 Mpc – and to  $\sim 1$  Abell radius – in our concordance cosmology).

Applying the above analysis, we find a projected virial radius  $R_{\text{vir}} = 1.9\text{ Mpc}$ , and a virial mass  $M_{\text{vir}} = 4.1 \times 10^{15} M_{\odot}$ .

However, we have to take into account that our observations cover a large part of the cluster, but not the whole cluster: the value of  $M_{\text{vir}}$  represents a good estimate of the mass only within our observational window, but not of the total mass. In a given cosmology, the total virialized mass of a cluster is expected to be correctly estimated if the ratio  $\Delta_{\text{vir}} \equiv \bar{\rho}(r_{\text{vir}})/\rho_c(z)$  of the mean density within  $r_{\text{vir}}$  to the critical density is lower than a given value  $\Delta_c$ , which depends on the cosmological model and the cluster redshift. The value of  $\Delta_c$  can be derived in the spherical collapse model assuming that the cluster has just virialized: in the case of an Einstein-de Sitter model,  $\Delta_c = 18\pi^2$ , usually approximated with  $\Delta_c = 200$ , while in our cosmology  $\Delta_c = 97$  at  $z = 0$  (see e.g. Eke et al. 1996) and  $\Delta_c = 118$  at  $z = 0.2$  (using the fitting formula in Bryan & Norman 1998); for sake of comparison we will give values both for  $\Delta_c = 100$  and  $\Delta_c = 200$ .

Given that  $\rho_c(z) = 3H(z)^2/8\pi G$  and  $H(z) = H_0[\Omega_M(1+z)^3 + \Omega_k(1+z)^2 + \Omega_\Lambda]^{1/2}$ ,  $\Delta_{\text{vir}}$  can be related to the virial radius according to the relation:

$$\frac{\bar{\rho}(r_{\text{vir}})}{\rho_c(z)} = \frac{1}{\rho_c(z)} \frac{3M_{\text{vir}}}{4\pi r_{\text{vir}}^3} = \frac{\sigma_r^2}{r_{\text{vir}}^2} \frac{6}{H^2(z)}. \quad (5)$$

Introducing the mean cluster redshift and the estimated value of the three-dimensional virial radius into the above equation, with  $r_{\text{vir}} = \pi R_{\text{vir}}/2 = 2.8$ , we find  $\Delta_{\text{vir}} \sim 250$ . As expected, this value is higher than  $\Delta_c$ . In order to measure the total mass, we have therefore to extrapolate  $M_{\text{vir}}$  to larger radii.

Assuming that at radii larger than  $r_{\text{vir}}$  the profile behaves as  $\rho(r) \propto r^{-\alpha}$ , from Eq. (5) we find the radius  $r_{\Delta_c}$  within which the mean density is  $\Delta_c \rho_c(z)$ :

$$r_{\Delta_c} = \frac{\sqrt{6}\sigma_r}{H(z)} \frac{\Delta_{\text{vir}}^{\frac{1}{\alpha}-\frac{1}{2}}}{\Delta_c^{\frac{1}{\alpha}}}. \quad (6)$$

The mass goes as  $M(r) \propto r^{3-\alpha}$  if  $\alpha \neq 3$ , or  $M(r) \propto \ln r$  if  $\alpha = 3$ . For  $\alpha \neq 3$  we obtain

$$M_{\Delta_c} = M_{\text{vir}} \left( \frac{\Delta_{\text{vir}}}{\Delta_c} \right)^{1/\alpha}. \quad (7)$$

Assuming  $\alpha = 4$ , which corresponds to an Hernquist profile at large radii (Hernquist 1990) and gives a convergent mass, we find  $r_{100} = 3.6$  Mpc and  $r_{200} = 3.1$  Mpc, while  $M_{100} = 5.0$  and  $M_{200} = 4.2 \times 10^{15} M_{\odot}$ .

Until now we have ignored the surface pressure term (The & White 1986). This is an additional term to the standard virial theorem which must be taken into account when the volume used to estimate the virial mass does not include the whole system. Neglecting it, the virial mass is overestimated by a factor depending on the observed fraction of the cluster and its profile; this factor cannot be larger than 50%, which is the case of an isothermal sphere (see Carlberg et al. 1996; Girardi et al. 1998). In our case, the field is quite large and the expected surface pressure term should be small, but in order to quantitatively assess the effect of the field size we have used numerical simulations. We have generated 1000 mock clusters, each one following an Hernquist distribution, with a density profile truncated at 20 Mpc and  $R_e \sim 1.8153a = 1$  Mpc. We have chosen this value as Lanzoni et al. (2004) have found that for cluster dark haloes the half-mass projected radius is in the range of 0.2 to 0.4  $r_{100}$ : the estimated value of  $r_{100} = 3.6$  Mpc for A 2163 implies that  $R_e$  should be between  $\sim 0.7$  and 1.4 Mpc. The total mass has been fixed to  $3.5 \times 10^{15} M_{\odot}$ , a value slightly smaller than estimated which reproduces the observed velocity dispersion; the average number of simulated galaxies has been chosen to reproduce – on the average – the observed number of cluster members. We have estimated the virial radii and masses of the simulated clusters as a function of the field radius, applying the same analysis as for the real data. The dispersion of the mass values around the mean gives an estimate of the error due to the Poissonian sampling, while the systematic offset of the measured mean mass with respect to the prediction for a theoretical Hernquist profile gives an estimate of the surface pressure term. The average measured virial mass of the simulations within 10 arcmin is  $2.75 \pm 0.25 \times 10^{15} M_{\odot}$ , i.e. 79% of the total mass, with a  $1\sigma$  error of 9%. According to the theoretical Hernquist profile with a cutoff at 20 Mpc, we would expect 71% of the total mass within 10 arcmin, i.e. on average we overestimate the mass of the simulated cluster by 8%.

Taking into account the pressure term, we find  $M_{\text{vir}} = 3.8 \pm 0.4 \times 10^{15} M_{\odot}$ , while the extrapolated total masses are  $M_{200} = 3.9 \pm 0.4 \times 10^{15} M_{\odot}$  and  $M_{100} = 4.6 \pm 0.5 \times 10^{15} M_{\odot}$ . Our values are in good agreement with the X-ray estimate of Elbaz et al. which, rescaled to  $H_0 = 70 \text{ km s}^{-1} \text{ Mpc}^{-1}$ , corresponds to  $3.3 \times 10^{15} M_{\odot}$  within  $r = 3.3$  Mpc, and confirm that A 2163 is one of the most massive clusters known.

## 7. Discussion and conclusions

Multiple signatures of merging have been detected in A 2163. Comparing this optical analysis to previous results at other

wavelengths allows important clues concerning the merging history of this cluster to be derived.

A 2163 appears to be composed of a main component (A 2163-A), and a subcluster 7' North of its center (A 2163-B), both identified at optical and X-ray wavelengths, and of various clumps: A 2163-C, A 2163-D, and A 2163-E, East, West and South of the main component respectively, detected only in the optical. A 2163-A, A 2163-B and A 2163-C are spectroscopically confirmed. A large scale elongation extending over 20 arcmin (4 Mpc) along the E-W direction, in which A 2163-A, A 2163-C and A 2163-D are embedded, appears at faint magnitudes. A bridge of faint galaxies appears to connect A 2163-A to A 2163-B along the North-South direction. A 2163-E also lies on this N-S axis. The central cluster A 2163-A shows a strong luminosity segregation in its projected density distribution. At bright magnitudes, there is a NE/SW structure, with a bright maximum in the NE part and a secondary maximum in the SW part. When including galaxies at fainter magnitudes, the orientation of the inner subclustering changes, showing two maxima aligned in the E-W direction. We find that there are relative offsets in the positions of: a) the BCGs; b) the peaks in the projected galaxy density maps; c) the X-ray density peak. Restricting the analysis to the members of the red-sequence shows the same properties, while enhancing the density contrast of the bimodal structure in the central part of A 2163-A.

Another signature of merging is the presence of multimodality in the velocity distribution of the whole cluster. With a KMM analysis we identify two partitions very close in velocity, centered at  $59\,186 \text{ km s}^{-1}$  (KMM1) and  $60\,545 \text{ km s}^{-1}$  (KMM2), respectively, corresponding to the two main peaks in the velocity histogram, and a third partition peaked at  $62\,410 \text{ km s}^{-1}$  (KMM3). The spatial distribution of the galaxies belonging to the KMM1 and KMM2 partitions is different; in particular in the central region KMM1 galaxies lie preferentially in the NE while KMM2 galaxies tend to populate the central region. Galaxies in the KMM3 partition do not show any particular concentration and are distributed along an elongated structure, following the main E-W axis of the cluster.

A comparison of the optical and X-ray density maps indicates a strong segregation between gas and galaxies, and interesting alignment effects. In A 2163-A, the main NE/SW axis joining the two maxima in the isodensity map of bright galaxies is nearly aligned with the inner direction in the gas density contours, and is perpendicular to the compression of the X-ray isophotes in the SW region. This can be expected in the case of merging between these two clumps along a NE/SW axis. On the other hand, at larger scales the gas density distribution is mostly oriented along an East-West axis, which is also the case for the large-scale over-density embedding A 2163-A, A 2163-C and A 2163-D, and for the density distribution of faint galaxies of A 2163-A.

Several facts argue that we are witnessing a post-merger event: for instance the relatively mixed velocity distribution (Schindler & Böhringer 1993), and the location of the X-ray gas density maximum between the two peaks of the galaxy density distribution. The most likely scenario for the main cluster is that a collision has already occurred within A 2163-A, as suggested by Elbaz et al. (1995) & Squires et al. (1997). The two density clumps existing in the core of the galaxy distribution would be the fossils of the previously colliding subclusters. Another signature of a post-merger event is the luminosity segregation detected in A 2163-A. A luminosity segregation in projected density has been observed in several observed clusters (Biviano et al. 1996; Barrena et al. 2007). The most luminous cluster galaxies are then

supposed to trace the remnants of the pre-merging substructures, while the distribution of fainter objects, elongated in the same direction as the ICM distribution, traces the large-scale structure and morphology of the recently formed cluster. Moreover, in A 2163-A the velocity distribution of bright objects ( $R < 19$ ) is more dispersed than that of fainter objects ( $19 < R < 21$ ), varying from  $\sim 1800 \text{ km s}^{-1}$  to  $\sim 1200 \text{ km s}^{-1}$ . The density distribution of those faint objects with measured redshift also coincides roughly with that of the gas shown by X-ray isocontours, but this result may be affected by incomplete spectroscopy sampling at faint magnitudes. These facts suggest that the distribution of faint objects is quietly settling within the cluster potential, while that of bright objects is still substantially disturbed, as expected in the early period after a merger.

The comparison with the dark matter and gas density maps derived from numerical simulations is essential in order to constrain the merging scenario, in particular the epoch and the axis of the merger event. This is due to the difference in relaxation times between the collisionless (dark matter and galaxies) and collisional (gas) components of the cluster. Roettiger et al. (1997) have followed the evolution of gas density and dark matter density distributions during the merging process. While gas and dark matter contours are coincident before the merging, they become quite different after core passage, with the gas “sloshing” about within the gravitational potential. The observed relative distribution of gas and galaxies in A 2163-A, with a single peak in the X-ray gas contours located in between the two peaks of the galaxy distribution is quite similar to that observed in simulations immediately ( $\sim 0.5$  Gyr) after the merger (see Fig. 23c of Roettiger et al. 1997). Chandra observations (Markevitch et al. 2001; Govoni et al. 2004) at higher spatial resolution indicate a possible X-ray double peak structure in the very center of A 2163. However the separation of these peaks ( $\leq 5$  arcsec) is much smaller than that shown by the galaxy distribution, and their positions still lie between the galaxy density peaks.

Subclustering tests can also bring information on the merging axis. From numerical simulations Pinkney et al. (1996) conclude that if the angle between the merger axis and the line of sight is greater than 30 degrees, little substructure will be detected in the 1D velocity distribution during the 2 Gyr following the merger. We detect subclustering in A 2163 not only with 2D and 3D tests, but also from the analysis of the radial velocity distribution (strong velocity gradient). This implies that the merging axis (whose projection on the plane of the sky follows the NE/SW direction) also contains a component along the line of sight, and that the angle of the merger axis with the line of sight should be less than 30 degrees. It is interesting to note the spatial coincidence between the SW clump A2 revealed at bright magnitudes, and the cold core detected by Govoni et al. (2004) in the Chandra temperature map, near the region of compressed X-ray contours.

Some facts still remain to be explained. A priori, one would have expected a correlation between the position of the BCGs and the two density peaks A1 and A2, defined by bright galaxies. The Eastern BCG1, is located near the NE bright clump A1. However, the location of BCG2, which is completely offset to the West side of A 2163-A, is quite puzzling. However, in case of a post-merger event, such apparent discrepancies can be expected. The velocities of the two BCGs are comparable to the cluster mean velocity and are within the range defined by the two central velocity peaks: they have respective offsets of  $+230 \text{ km s}^{-1}$  and  $-125 \text{ km s}^{-1}$  with respect to the global cluster velocity derived from the high precision sample, which correspond to physical

velocity differences of  $+192 \text{ km s}^{-1}$  and  $-104 \text{ km s}^{-1}$  in the reference system of the cluster.

Another issue is the geometry of the merging event. While the projected density distribution of bright galaxies ( $R < 19$ ) suggests a NE/SW axis, the two BCGs and the projected density distribution of the fainter galaxies are aligned along a E-W axis. The analysis of the velocity distribution of bright galaxies seems to confirm the NE/SW orientation for the merger axis, and that of fainter galaxies appears to be consistent. However, one has to note that the velocity distribution of the fainter objects is very poorly sampled, especially in the western subcluster of A 2163-A, visible in the projected density map at  $R < 21$ , and responsible of the twist of the isophotes from NE/SW to E-W. Important issues on the velocity distribution of faint galaxies may therefore be hidden by this inhomogeneous sampling. A detailed analysis of the density and temperature distribution of the gas from XMM observations, and of the further constraints on the merging scenario which can be derived from a comparison to numerical simulations will be presented in a forthcoming paper.

The northern component A 2163-B is shown from our spectroscopic analysis to lie at a redshift comparable to that of the main cluster, so it is part of the same complex. This confirms the photometric redshift analysis of La Barbera et al. (2004). However, the velocity distribution is complex, with three velocity peaks and a high velocity dispersion, more typical of a rich cluster than of a group. Part of this high dispersion might be due to contamination from galaxies of the main cluster.

A possible scenario is that A 2163-B is infalling towards A 2163-A. This pre-merger hypothesis is consistent with the shape and coincidence of the gas and bright galaxy density distributions. However, two features are not easily explained: the fact that at fainter magnitudes the projected density distribution of A 2163-B shows a significant Western trail (confirmed by the redshift space density maps) which seems to extend towards A 2163-A through a N-S bridge of galaxies, and that the velocity distribution appears highly dispersed. While the high velocity dispersion may be an artifact due to an insufficient spectroscopic sampling, the N-S bridge of galaxies is not explained in this scenario.

This bridge could in fact have a tidal origin. Another scenario is that A 2163-B has already undergone a high impact parameter merging event with A 2163-A. Crossing the very peripheral region of A 2163-A, the gas core would have been preserved, but the tidal interaction would have left the N-S bridge of faint galaxies. Moreover, the velocity dispersion of A 2163-B would have been strongly increased by the merging event. This scenario is however difficult to reconcile with present X-ray observations, since whatever the impact parameter, one should in principle detect a trailing emitting X-ray gas, which is not the case. Deeper study of the X-ray observations, in combination with the present data, should help to resolve the issue.

The Eastern and Western clumps, A 2163-C and A 2163-D, less dense than A 2163-B and not visible in X-ray, are likely to be groups infalling towards A 2163-A along the E-W structure. The presence of a significant excess of emission line galaxies in the Western periphery of A 2163-D could also be related to the merging process, which has been suggested to trigger a burst of star formation in the galaxy population (Bekki 1999), or to accretion on the E-W filament. The southern clump A 2163-E is probably accreting in the N-S direction.

Although the central region of the cluster exhibits clear signatures of recent merging, the velocity distribution on the whole sampled region is not statistically deviant from a Gaussian distribution, and the averaged density profiles are reasonably

regular. Therefore it appears reasonable to estimate the mass by application of the virial theorem: the resulting value,  $M_{\text{vir}} = 3.8 \pm 0.4 \times 10^{15} M_{\odot}$ , is among the largest measured for a cluster. This would remain true even taking into account the uncertainties which could cause an overestimate of the mass ( $\sim 25\%$  if for example the true velocity dispersion were as low as found for the subsample of the central, faint galaxies, i.e.  $\sim 1200 \text{ km s}^{-1}$ ).

In conclusion, the observed properties of A 2163 result from multiple merging and accretion processes. We should probably speak of an “A 2163 complex”, a very massive structure composed of a main component having recently undergone a strong merger phase along the NE/SW or E-W axis with a velocity gradient  $\sim 1500 \text{ km s}^{-1}$ , accreting a variety of groups aligned along a large scale filament spreading over 4 Mpc in the E-W direction. The secondary northern subcluster A 2163-B belongs to the same complex and according to optical observations alone has probably already crossed the periphery of A 2163-A.

*Acknowledgements.* The data published in this paper have been reduced using VIPGI, designed by the VIRMOS Consortium and developed by INAF Milano. We thank Bianca Garilli for her generous help, together with Marco Scodreggio, Paolo Franzetti and Luigi Paioro for numerous interactions in the VIPGI data reduction. We thank the Programme National de Cosmologie of CNRS for his constant support on this program, the Observatoire de la Côte d’Azur and the Laboratoire Cassiopée, CNRS, for funding this project. We are very grateful to Luigina Feretti for fruitful discussions. We also thank Eric Slezak and Albert Bijaoui for providing the density estimator based on the Multiscale Vision Model used in this paper. We thank Andrea Biviano, José de Freitas Pacheco and Heinz Handernach for their reading of the manuscript and for their comments. We thank the referee for his/her useful comments which helped to improve the quality of this paper. CF acknowledges financial support of Austrian Science Foundation (FWF) through grant number P18523, and Tiroler Wissenschaftsfonds (TWF) through grant number UNI-0404/156. GWP acknowledges support from DFG Transregio Programme TR33. H.B. acknowledges the financial support from contract ASI-INAF I/023/05/0.

## References

- Adami, C., Mazure, A., Ulmer, M. P., & Savine, C. 2001, *A&A*, 371, 11  
 Arnaud, M., Hughes, J. P., Forman, W., et al. 1992, *ApJ*, 390, 345  
 Arnaud, M., Maurogordato, S., Slezak, E., & Rho, J. 2000, *A&A*, 355, 461  
 Ashman, K. M., Bird, C. M., & Zepf, S. E. 1994, *AJ*, 108, 2348  
 Barrena, R., Boschin, W., Girardi, M., & Spolaor, M. 2007, *A&A*, 469, 861  
 Bardelli, S., Zucca, E., & Baldi, A. 2001, *MNRAS*, 320, 387  
 Beers, T. C., Flynn, K., & Gebhardt, K. 1990, *AJ*, 100, 32  
 Beers, T. C., Forman, W., Huchra, J. P., Jones, C., & Gebhardt, K. 1991, *AJ*, 102, 1581  
 Bekki, K. 1999, *ApJ*, 510, L15  
 Bertin, E., & Arnouts, S. 1996, *A&AS*, 117, 393  
 Bird, C. M., & Beers, T. C. 1993, *AJ*, 105, 1596  
 Bird, C. 1994, *ApJ*, 422, 480  
 Biviano, A., Murante, G., Borgani, S., et al. 2006, *A&A*, 456, 23  
 Boschin, W., Girardi, M., Barrena, R., et al. 2004, *A&A*, 416, 839  
 Boschin, W., Girardi, M., Spolaor, M., & Barrena, R. 2006, *A&A*, 449, 461  
 Bottini, D., Garilli, B., Maccagni, D., et al. 2005, *PASP*, 117, 996  
 Bourdin, H., Slezak, E., Bijaoui, A., & Arnaud, M. 2001, *Proc. of the XXXVth Rencontres de Moriond, XX1st Moriond Astrophysics Meeting*, March 10–17, 2001 Savoie, France, ed. D. M. Neumann, J. Tran Thanh Van [arXiv:astro-ph/0106138]  
 Brunetti, G. 2003, *ASP Conf. Ser.*, 301, 349 [arXiv:astro-ph/0208074]  
 Bruzual, G., & Charlot, S. 2003, *MNRAS*, 344, 1000  
 Bryan, G. L., & Norman, M. L. 1998, *ApJ*, 495, 80  
 Carlberg, R. G., Yee, H. K. C., Ellington, E., et al. 1996, *ApJ*, 462, 32  
 Coleman, G., Wu, C., & Weedman, D. 1980, *ApJS*, 43, 393  
 Czoske, O., Moore, B., Kneib, J.-P., & Soucail, G. 2002, *A&A*, 386, 31  
 Cypriano, E. S., Sodr , L. Jr., Kneib, J. P., & Campusano, L. E. 2004, *ApJ*, 613, 108  
 den Hartog, R., & Katgert, P. 1996, *MNRAS*, 279, 349  
 Dressler, A., & Shectman, S. 1988, *AJ*, 95, 985  
 Elbaz, D., Arnaud, M., & B hringer, H. 1995, *A&A*, 293, 337  
 Eke, V. R., Cole, S., & Frenk, C. S. 1996, *MNRAS*, 282, 263  
 Everitt, B. S., & Hand, D. J. 1981, *Finite mixture distributions* (Chapman, Hall)  
 Fadda, D., Slezak, E., & Bijaoui, A. 1998, *A&AS*, 127, 335  
 Ferrari, C., Maurogordato, S., Cappi, A., & Benoist, C. 2003, *A&A*, 399, 813  
 Ferrari, C., Benoist, C., Maurogordato, S., Cappi, A., & Slezak, E. 2005, *A&A*, 430, 19  
 Ferrari, C., Govoni, F., Schindler, S., Bykov, A. M., & Rephaeli, Y. 2008, *SSR*, in press  
 Feretti, L. 2006, *Proceeding of XL1st Rencontres de Moriond, XXVth Astrophysics Moriond Meeting: From dark halos to light*, ed. L. Tresse, S. Maurogordato, J. Tran Thanh Van, [arXiv:astro-ph/0612185]  
 Feretti, L., Fusco-Femiano, R., Giovannini, G., & Govoni, F. 2001, *A&A*, 373, 106  
 Feretti, L., Orru, E., Brunetti, G., et al. 2004, *A&A*, 423, 11  
 Flores, R. A., Quintana, H., & Way, M. J. 2000, *ApJ*, 532, 206  
 Girardi, M., Giuricin, G., Mardirossian, F., Mezzetti, M., & Boschin, W. 1998, *ApJ*, 505, 74  
 Girardi, M., Demarco, R., Rosati, P., & Borgani, S. 2005, *A&A*, 442, 29  
 Girardi, M., Boschin, W., & Barrena, R. 2006, *A&A*, 455, 45  
 Giovannini, G., & Feretti, L. 2002, *Merging Processes in Galaxy Clusters*, ed. L. Feretti, I. M. Gioia, G. Giovannini, *Astrophysics and Space Science Library* (Dordrecht: Kluwer Academic Publishers), 272, 197  
 Gonzalez-Casado, G., Mamon, G. A., & Salvador-Sole, E. 1994, *ApJ*, 433, L61  
 Govoni, F., Markevitch, M., Vikhlinin, A., et al. 2004, *ApJ*, 605, 695  
 Henriksen, M., Donnelly, R. H., & Davis, D. S. 2000, *ApJ*, 529, 692  
 Hernquist, L. 1990, *ApJ*, 356, 359  
 La Barbera, F., Merluzzi, P., Busarello, G., Massarotti, M., & Mercurio, A. 2004, *A&A*, 425, 797  
 Lanzoni, B., Ciotti, L., Cappi, A., Tormen, G., & Zamorani, G. 2004, *ApJ*, 600, 640  
 Ledlow, M. J., Owen, F. N., & Miller, N. A. 2005, *AJ*, 130, 47  
 Le F vre, O., Saisse, M., Mancini, D., et al. 2000, *SPIE Proc.*, 4008, 546  
 L pez-Cruz, O., Barkhouse, W. A., & Yee, H. K. C. 2004, *ApJ*, 614, 679  
 Lubin, L. M., & Bahcall, N. A. 1993, *ApJ*, 415, L17  
 Markevitch, M., & Vikhlinin, A. 2001, *ApJ*, 563, 95  
 Maurogordato, S., Proust, D., Beers, T. C., et al. 2000, *A&A*, 355, 848  
 McLachlan, G. J., & Basford, K. E. 1988, *Mixture Models* (New York: Marcel Dekker)  
 Miller, N. A., Owen, F. N., Hill, J. M., et al. 2004, *ApJ*, 613, 841  
 Miller, N. A., Oegerle, W., & Hill, J. M. 2006, *ApJ*, 131, 2426  
 Pinkney, J., Roettiger, K., & Burns, J. O. 1996, *ApJS*, 104, 1  
 Popesso, P., Bohringer, H., Romaniello, M., et al. 2005, *A&A*, 433, 415  
 Pratt, G., Arnaud, M., & Aghanim, N. 2001, [arXiv:astro-ph/0105431]  
 Quintana, H., Ramirez, A., & Way, M. J. 1996, *AJ*, 112, 36  
 Ricker, P. M., & Sarazin, C. L. 2001, *ApJ*, 561, 621R  
 Roettiger, K., Loken, C., & Burns, J. O. 1997, *ApJ*, 109, 307  
 Schindler, S., & B hringer, H. 1993, *A&A*, 269, 83  
 Schlegel, D. J., Finkbeiner, D. P., & Davis, M. 1998, *ApJ*, 500, 525  
 Scodreggio, M., Franzetti, P., Garilli, B., et al. 2005, *PASP*, 117, 1284  
 Slezak, E. 2007, in preparation  
 Squires, G., Neumann, D., Arnaud, M., et al. 1997, *ApJ*, 482, 648  
 Tonry, J., & Davis, M. 1981, *ApJ*, 246, 666  
 Vandame, B. 2002, *SPIE Proc.*, 4847, 123  
 Yahil, A., & Vidal, N. V. 1977, *ApJ*, 214, 347  
 Yasuda, N., Fukugita, M., Narayanan, V. K., et al. 2001, *AJ*, 122, 1104  
 West, M. J., & Bothun, G. D. 1990, *ApJ*, 350, 36